

<https://doi.org/10.1038/s41534-025-01147-1>

Photon-number conserved universal quantum logic employing continuous-time quantum walk on dual-rail qubit arrays

Check for updates

Hao-Yu Guan^{1,2,5}, Yifei Li^{3,5} & Xiu-Hao Deng^{1,2,4} ✉

We demonstrate a synergy between dual-rail qubit encoding and continuous-time quantum walks (CTQW) to realize universal quantum logic in superconducting circuits. Utilizing the photon-number-conserving dynamics of CTQW on dual-rail transmons, which systematically transform leakage and relaxation into erasure events, our architecture facilitates the suppression of population leakage and the implementation of high-fidelity quantum gates. We construct single-, two-, and three-qubit operations that preserve dual-rail encoding, facilitated by tunable coupler strengths compatible with current superconducting qubit platforms. Numerical simulations confirm robust behavior against dephasing, relaxation, and imperfections in coupling, underscoring the erasure-friendly nature of the system. This hardware-efficient scheme thus provides a practical pathway to early fault-tolerant quantum computation, laying the groundwork for scalable gate implementations and advanced error-correction strategies.

In quantum information processing, high-fidelity control and error correction are vital, as superconducting architectures often suffer from leakage out of the logical subspace or relaxation to lower-energy states. A promising path to address these issues is converting leakage or relaxation events into erasure errors, which explicitly flag themselves for correction^{1,2}. Recent studies on dual-rail qubits encode information in a single photon-number excitation distributed across two resonantly coupled transmons, enabling efficient leakage detection and improving error-correction thresholds^{3–10}. Despite these advances in error detection capabilities, a critical gap persists in developing universal quantum logical gates that inherently preserve the dual-rail encoding during operation. This fundamental limitation currently constrains the practical implementation of fault-tolerant quantum computation using this promising architecture.

In parallel, continuous-time quantum walks (CTQW) provide a powerful framework that preserves the total number of excitations, making them a natural match for dual-rail encoding. By confining the walker—a single excitation—to a well-defined subspace, CTQW safeguards against leakage while enabling potential quantum speedups in hitting and mixing processes^{11–14}. These features have spurred experimental demonstrations across various integrated qubit systems, such as superconducting qubits^{15–17}. Beyond single-particle dynamics, interactions between multiple walkers introduce richer correlated behavior^{18,19} and can support robust quantum search^{20–23} and error correction²⁴. From a theoretical standpoint,

multi-walkers CTQW can construct universal quantum logic^{25,26}, supported by proposals demonstrating high-fidelity controlled-phase (CPhase) gates²⁷ or leveraging two internal states of the walker on a directed graph²⁸. A controlled-NOT (CNOT) gate has been constructed for both non-interacting bosons—realized by photons in waveguide lattices—and for interacting bosons using ultra-cold atoms²⁹. All these advancements highlight the potential of CTQW in universal quantum computing.

By integrating the dual-rail transmon encoding with CTQW, it is possible to harness the advantages of both methodologies: robust error management via erasure conversion and the preservation of photon-number properties inherent to CTQW. This integration enhances the efficiency of erasure error correction in quantum computing architectures built upon this framework. In this study, we propose a foundational framework to implement universal quantum logic based on the operation of correlated CTQW within the structure of dual-rail encoded qubit arrays. We present explicit constructions of single- and two-qubit gates, such as the controlled-Z (CZ) and iSWAP gates, alongside three-qubit gates, maintaining the dual-rail encoding by the end of the quantum evolution. Our analysis encompasses both transverse and longitudinal connections within a superconducting qubit array, deriving parameter regimes that align with current experimental methodologies utilizing tunable transmon couplers. Additionally, we investigate the behavior of these gate constructions under realistic noise conditions, including dephasing, relaxation, and imperfections in

¹International Quantum Academy, Shenzhen, China. ²Shenzhen Institute for Quantum Science and Engineering, Southern University of Science and Technology, Shenzhen, China. ³Cuiying Honors College, Lanzhou University, Lanzhou, China. ⁴Shenzhen Branch, Hefei National Laboratory, Shenzhen, China. ⁵These authors contributed equally: Hao-Yu Guan, Yifei Li. ✉ e-mail: dengxiuhao@iqasz.cn

coupler strengths or detunings. Our results suggest that the intrinsic properties of dual-rail transmons, in conjunction with the excitation-conserving attributes of CTQW, render this approach not only feasible but potentially robust against prevalent hardware imperfections. This comprehensive perspective holds promise for advancing early efforts in fault-tolerant quantum computation by providing both practical means for gate synthesis and a stable encoding architecture for superconducting circuits.

Results

Continuous-time quantum walks on the extended Bose-Hubbard model

The extended Bose-Hubbard model (EBHM) serves as a nontrivial model for studying quantum walks. There is no additional interaction energy when there is a single walker on graphs; when multiple walkers are on the same graphs, they interact with each other and exhibit correlated quantum walks²⁹. These quantum walks go beyond simple hopping, incorporating local phase shifts, on-site interactions, and nearest-neighbor correlations associated with EBHM. This subsection introduces the EBHM and its graph-based interpretation as a platform for describing such nontrivial CTQWs.

The EBHM incorporates additional interactions beyond the standard Bose-Hubbard framework, enabling the study of diverse quantum phenomena³⁰. It has been experimentally realized in ultracold atoms in optical lattices³¹, Rydberg atom arrays^{32,33}, superconducting circuits^{5,34}, and dipolar excitons³⁵.

In this work, we implement the EBHM using a two-dimensional superconducting circuit composed of transmons and tunable couplers, as illustrated in Fig. 1(a). Starting from the full circuit Hamiltonian, we derive an effective Hamiltonian by decoupling the coupler. This effective Hamiltonian is then transformed into the rotating frame. The full description of

the superconducting circuit and technical details are provided in the Methods section. As a result, we obtain the EBHM Hamiltonian^{36,37}:

$$\hat{H} = -J \sum_{(i,j)} \hat{c}_i^\dagger \hat{c}_j + \frac{U}{2} \sum_i \hat{n}_i (\hat{n}_i - 1) - \sum_i \mu_i \hat{n}_i + V \sum_i \hat{n}_i \hat{n}_{i+1}, \quad (1)$$

where $\hat{c}_i^{(\dagger)}$ annihilates (creates) a boson at site i , $\hat{n}_i \equiv \hat{c}_i^\dagger \hat{c}_i$ is the number operator. The parameters J , U , μ_i , and V denote the tunneling amplitude, on-site interaction strength, chemical potential, and nearest-neighbor interaction strength, respectively.

In this context, a graph $G = (V_G, E)$ is defined, where V_G represents the lattice sites (vertices) and E denotes the edges that correspond to specific Hamiltonian terms. To visually represent the physical processes described by the Hamiltonian, we employ the following color coding:

- Blue edges: Correspond to the tunneling term $(-J \sum_{(i,j)} \hat{c}_i^\dagger \hat{c}_j)$ and describe particle hopping between neighboring sites.
- Orange edges: Represent the chemical potential term $(-\mu \sum_i \hat{n}_i)$ and capture local phase accumulation or energy shifts.
- Red edges: Represent the nearest-neighbor interaction term $(V \sum_i \hat{n}_i \hat{n}_{i+1})$, modeling interactions between particles at adjacent sites.

To align with superconducting circuit implementations, we will henceforth refer to these terms as the coupling, frequency shift (detuning), and ZZ interaction terms, respectively. The detailed settings on the superconducting circuit are elaborated in Section I of the Supplementary Note.

In the language of CTQWs, these edges describe distinct types of quantum walks, as depicted in Fig. 1(b):

- Translational walk: (blue edges) A walker hops from one site to another.
- Loop-back walk: (orange edges) A walker remains confined to a single site and accumulates phase, analogous to self-loops in a graph.
- Collision walk: (blue + red edges) Neighboring walkers exchange sites with interaction, resulting in a correlated quantum walk.
- Collision: (red edges) Neighboring walkers interact, resulting in pure interaction.

Each graph G can be transformed into a dual graph, which encodes the structure of couplings and interactions among the Fock states governed by the Hamiltonian. This dual graph provides an intuitive graphical representation of the transitions facilitated by the Hamiltonian terms, illustrating how quantum states interact and evolve.

This graph-based approach opens pathways for studying many-body quantum dynamics and correlations in a controlled experimental setting.

Dual-rail encoding on a graph

In this subsection, we describe a dual-rail encoding scheme in the EBHM, where single microwave-photon excitations (“walkers”) propagate on a graph G . This encoding exploits the spatial delocalization of the walker to represent logical qubits across pairs of adjacent transmons. We introduce the logical and complementary subspaces, discuss the total Hilbert space dimension, and explain the default system configuration used for qubit initialization.

As depicted in Fig. 1, a single walker occupying two longitudinally adjacent transmons constitutes a logical qubit. The logical states $|0\rangle_L$ and $|1\rangle_L$ are defined by the excitation (walker) being localized in the upper or lower site, respectively. In a superposition, the walker delocalizes across these two sites, enabling qubit encoding without additional degrees of freedom.

We now describe how to encode logical qubits using a Hamiltonian graph G composed of $2n$ transmons arranged in a $2 \times n$ array. We label the transmon vertices as $v_{i,x}$ where $i \in \{1, \dots, n\}$ indexes the columns and $x \in \{0, 1\}$ indexes the rows. In each column i , the vacuum state is defined as

$$|\text{vac}_i\rangle = |0_{i,0}0_{i,1}\rangle. \quad (2)$$

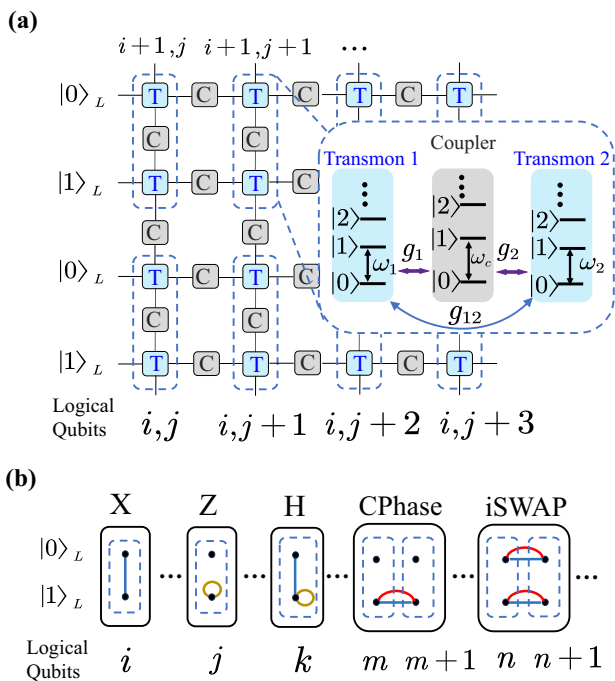


Fig. 1 | Illustration of the dual-rail encoded qubit array and logical operations. **a** A building block of a 4×2 logical qubits array. Each logical qubit (dashed boxes) consists of two transmons (blue boxes) and one coupler (gray boxes). The coupling scheme is illustrated in the inset dashed box. **b** Quantum walks on various graphs represent different logical operations on the 1-D logical qubit array, with corresponding gates marked above the solid boxes. Each vertex corresponds to a transmon, while a pair of transmons in the dashed box indicates an encoded logical qubit. Blue, orange, and red edges signify translational, loop-back, and collision walks, respectively.

A single walker created at vertex $v_{i,x}$ is represented by $\widehat{c}_{i,x}^\dagger|\text{vac}_i\rangle$. We encode a logical qubit in the i -th column by using the presence of exactly one walker, with the logical basis states defined as

$$\begin{aligned} |0_i\rangle_L &\equiv |1_{i,0}0_{i,1}\rangle \equiv \widehat{c}_{i,0}^\dagger|\text{vac}_i\rangle, \\ |1_i\rangle_L &\equiv |0_{i,0}1_{i,1}\rangle \equiv \widehat{c}_{i,1}^\dagger|\text{vac}_i\rangle. \end{aligned} \tag{3}$$

Any logical state in the i -th column can then be written as

$$|\psi_i\rangle = \alpha|0_i\rangle_L + \beta|1_i\rangle_L. \tag{4}$$

Extending this to n columns, the logical Hilbert space \mathcal{H}_L for n qubits is defined as the tensor products of single logical qubit

$$\mathcal{H}_L = \text{span}\{|0_1\rangle_L|0_2\rangle_L \cdots |0_n\rangle_L, |0_1\rangle_L|0_2\rangle_L \cdots |1_n\rangle_L, \dots, |1_1\rangle_L|1_2\rangle_L \cdots |1_n\rangle_L\}. \tag{5}$$

A valid n -walker state $|\psi\rangle \in \mathcal{H}_L$ satisfies the condition that each column contains exactly one walker:

$$\sum_{x=0}^1 \langle \psi | \widehat{c}_{i,x}^\dagger \widehat{c}_{i,x} | \psi \rangle = 1, \forall i \in \{1, \dots, n\}. \tag{6}$$

Placing n independent bosonic walkers on $2n$ vertices generates a full Hilbert space

$$\mathcal{H} = \text{span}\left\{ \bigotimes_{i=1}^n |m_{i,0}m_{i,1}\rangle, m_{i,x} \in [0, n], \sum_{i,x} m_{i,x} = n \right\}, \tag{7}$$

with $m_{i,x} \in \mathbb{N}$ and dimension³⁸

$$\mathcal{D} = \binom{3n-1}{n} = \frac{(3n-1)!}{n!(2n-1)!} \approx 2.6^n, \tag{8}$$

which is substantially larger than the 2^n -dimensional logical space \mathcal{H}_L defined by the presence of exactly one walker per column. Consequently, the full Hilbert space can be decomposed as

$$\mathcal{H} = \mathcal{H}_L \oplus \mathcal{H}_\perp, \tag{9}$$

where \mathcal{H}_\perp denotes the complementary subspace. Any state $|\Psi\rangle$ with support in \mathcal{H}_\perp does not encode valid qubit information. Although a physical Hamiltonian may couple \mathcal{H}_L to \mathcal{H}_\perp and allow the walker to transiently explore \mathcal{H} , a well-defined gate time T ensures that the resulting unitary remains block-diagonal:

$$U = U_L \oplus U_\perp. \tag{10}$$

Hence, any state initially in \mathcal{H}_L returns to the logical subspace at the end of the evolution—despite possible temporary transitions into \mathcal{H}_\perp . This mechanism leverages the larger Hilbert space to generate entanglement, aided by bosonic indistinguishability³⁹.

By tuning the couplers' frequencies far from the transmons ($\Delta_1/2\pi \approx 3$ GHz), the system's default configuration consists of isolated transmons with both the coupling and ZZ interaction set to zero^{40,41}. Additionally, we set $\mu_i = 0$. In this default configuration without other operations, the system Hamiltonian is

$$\widehat{H}_0 = \frac{U}{2} \sum_{i=1}^n \sum_{x=0}^1 \widehat{n}_{i,x}(\widehat{n}_{i,x} - 1), \tag{11}$$

resulting in a disconnected graph of $2n$ vertices with no edges. Initializing the system in $|\psi\rangle = \bigotimes_{i=1}^n |0_i\rangle_L$ yields a zero-energy eigenstate of \widehat{H}_0 , ensuring no dynamics occur in the absence of applied operations.

Single-qubit gates

To provide a comprehensive overview, we begin with a brief introduction to single-qubit gate implementation before proceeding to the construction of two-qubit gates. Here, we demonstrate the implementation of single-qubit gates X, Z with arbitrary rotation angles, in addition to the Hadamard gate. The associated quantum walk graphs are illustrated in Fig. 1(b).

The Hamiltonian for the X gate applied to the i -th logical qubit is:

$$\widehat{H}_{X,i} = -J_X(\widehat{c}_{i,1}^\dagger \widehat{c}_{i,0} + \text{H.c.}) + \mu_X(\widehat{n}_{i,0} + \widehat{n}_{i,1}) + \widehat{H}_0, \tag{12}$$

where J_X is the coupling strength and μ_X is the frequency shift of the two physical qubits. When restricted to the two logical states $|0_i\rangle_L$ and $|1_i\rangle_L$, the Hamiltonian simplifies to $-J_X \widehat{\sigma}_x$, where $\widehat{\sigma}_x$ is the Pauli X operator. The corresponding gate time for the X -gate is:

$$T_X = \frac{\pi}{2J_X}. \tag{13}$$

The global phase induced by the coupling term can be canceled by setting $\mu_X = J_X$.

For the Z gate on the j -th logical qubit, the Hamiltonian becomes:

$$\widehat{H}_{Z,j} = -\mu_Z \widehat{n}_{j,1} + \widehat{H}_0, \tag{14}$$

where μ_Z represents the detuning applied to the site $(j, 1)$. The Hamiltonian in the logical subspace is:

$$\widehat{H}_{Z,j} = \begin{pmatrix} 0 & 0 \\ 0 & -\mu_Z \end{pmatrix}. \tag{15}$$

This Hamiltonian induces a phase shift on $|1_j\rangle_L$ at a rate $-\mu_Z$. The gate time for the Z -gate is:

$$T_Z = \frac{\pi}{\mu_Z}. \tag{16}$$

Since both X and Z gates do not couple states in \mathcal{H}_C to those in \mathcal{H}_\perp , they can be easily extended to arbitrary X -rotations $\widehat{R}_X(\theta) = e^{-i\theta \widehat{\sigma}_x}$, with gate time:

$$T_X(\theta) = \frac{2\pi - \theta}{J_X}, \tag{17}$$

and phase gates

$$P(\theta) = \begin{pmatrix} 1 & 0 \\ 0 & e^{i\theta} \end{pmatrix}, \tag{18}$$

with gate time:

$$T_P(\theta) = \frac{\theta}{\mu_Z}. \tag{19}$$

Arbitrary single-qubit gates can thus be implemented by decomposing rotations on the Bloch sphere using Euler angles⁴².

The Hadamard gate can be directly implemented on the k -th qubit using the Hamiltonian:

$$\widehat{H}_{H,k} = \mu_H \widehat{n}_{k,1} - J_H(\widehat{c}_{k,0}^\dagger \widehat{c}_{k,1} + \text{H.c.}) + \widehat{H}_0. \tag{20}$$

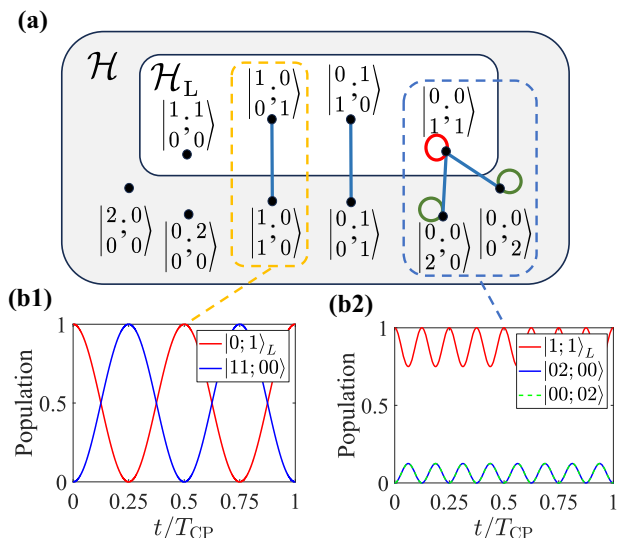


Fig. 2 | Dual graph and evolutions of the CPhase gate on dual-rail encoded qubits. **a** The graph describing the couplings and interactions among Fock states under the Hamiltonian \hat{H}_{CP} . The blue edges represent allowed couplings, the red self-loop denotes the ZZ interaction, and the green self-loops represent on-site interactions. **b** Population evolution of states within the dashed boxes in (a). The x-axis represents time in units of the gate time T_{CP} , and the y-axis shows the population of each state. The logical basis states return to their original population by the end of the gate time.

For $\mu_H/J_H = 2$, this Hamiltonian results in a Hadamard gate with a gate time:

$$T_H = \frac{\pi}{2\sqrt{2}J_H}. \tag{21}$$

This is more efficient than applying three separate decomposed single-qubit gates. The overall phase can be eliminated by adding a detuning term to both sites, with $\mu/J_H = \sqrt{2} - 1$.

CPhase gate for transverse connections

The realization of two-qubit gates involves activating one or two couplings in the system, thereby transiently linking the logical subspace \mathcal{H}_L with its orthogonal complement \mathcal{H}_\perp . A pivotal challenge is the precise determination of the gate duration T and the selection of an appropriate Hamiltonian, ensuring that by the conclusion of the operation, the state evolution remains confined to the logical subspace. As depicted in Fig. 1(a), the dual-rail encoded qubits positioned in a two-dimensional array showcase anisotropic interconnections. Transverse connections accommodate two coupling channels, whereas longitudinal connections possess a solitary coupling channel. This anisotropy necessitates distinct strategies for gate implementation, customized to the specific type of connection.

This subsection discusses the construction of the CPhase gate in transverse connections, leaving the longitudinal case for the next subsection. In particular, we show how a weak ZZ interaction can be utilized to implement a CZ gate in a superconducting circuit.

We begin by considering a 2×2 physical qubit block in a transverse connection for logical qubits, as shown in Fig. 1(b). In this subsection, we label the four vertices as $v_{i,0}$, $v_{i+1,0}$, $v_{i,1}$, and $v_{i+1,1}$. There are two available coupling channels between adjacent qubits: one between $v_{i,0}$ and $v_{i+1,0}$, and another between $v_{i,1}$ and $v_{i+1,1}$. These couplings are distinct from the longitudinal connection, which supports only a single coupling.

For the CPhase gate, we consider a system of two bosonic walkers on four lattice sites, resulting in a 10-dimensional Fock space \mathcal{H} . As shown in Fig. 2(a), the logical subspace \mathcal{H}_L is spanned by the following four

Fock states:

$$\begin{aligned} \hat{c}_{i,0}^\dagger \hat{c}_{i+1,0}^\dagger |00; 00\rangle &= |10; 10\rangle \leftrightarrow |0; 0\rangle_L, \\ \hat{c}_{i,0}^\dagger \hat{c}_{i+1,1}^\dagger |00; 00\rangle &= |10; 01\rangle \leftrightarrow |0; 1\rangle_L, \\ \hat{c}_{i,1}^\dagger \hat{c}_{i+1,0}^\dagger |00; 00\rangle &= |01; 10\rangle \leftrightarrow |1; 0\rangle_L, \\ \hat{c}_{i,1}^\dagger \hat{c}_{i+1,1}^\dagger |00; 00\rangle &= |01; 01\rangle \leftrightarrow |1; 1\rangle_L, \end{aligned} \tag{22}$$

where semicolons separate different logical columns. The remaining six states span the non-logical subspace (also given in Fig. 2)

$$\mathcal{H}_\perp = \text{span}\{|20; 00\rangle, |00; 20\rangle, |11; 00\rangle, |00; 11\rangle, |02; 00\rangle, |00; 02\rangle\}. \tag{23}$$

The CPhase gate is implemented by activating the coupling between the sites $(i, 1)$ and $(i + 1, 1)$ along with the ZZ interaction. Specifically, the frequency of the coupler between the two sites is tuned to be around $\Delta_1/2\pi \sim 1$ GHz. The system Hamiltonian is given by:

$$\hat{H}_{CP} = -J_{CP} (\hat{c}_{i,1}^\dagger \hat{c}_{i+1,1} + \text{H.c.}) + V_{CP} \hat{n}_{i,1} \hat{n}_{i+1,1} + \hat{H}_0, \tag{24}$$

where \hat{H}_0 is the default Hamiltonian of the system. Due to the nature of the ZZ interaction, the logical basis state $|1; 1\rangle_L$ experiences this interaction while the other three do not.

The evolution of the system is governed by the unitary operator $\hat{U}_{CP}(t) = \exp(-i\hat{H}_{CP}t)$. Since the logical state $|0; 0\rangle_L$ is decoupled from all other states, its evolution is trivial:

$$\hat{U}_{CP}(t)|10; 10\rangle = |10; 10\rangle. \tag{25}$$

For the second logical state $|0; 1\rangle_L$, we find that it couples to the non-logical state $|11; 00\rangle$. The evolution is given by:

$$\hat{U}_{CP}(t)|10; 01\rangle = \cos(J_{CP}t)|10; 01\rangle + i\sin(J_{CP}t)|11; 00\rangle. \tag{26}$$

To keep the state within the logical subspace, the evolution must be constrained by a specific gate time T_{CP} , which we define as:

$$T_{CP} = \frac{2\pi}{|J_{CP}|}. \tag{27}$$

Similar dynamics hold for the third logical state $|1; 0\rangle_L$. For the fourth state $|1; 1\rangle_L$, additional complexities arise as it couples to the non-logical states $|02; 00\rangle$ and $|00; 02\rangle$. These states will accumulate additional phases, either due to the on-site interaction or the ZZ interaction.

In summary, the evolution operator $\hat{U}_{CP}(t)$ can be decomposed into block diagonal form, with the Hamiltonian being block-diagonal within four invariant subspaces. We define these subspaces as:

$$\begin{aligned} \mathcal{H}_1 &= \{|0; 0\rangle_L\}, \\ \mathcal{H}_2 &= \text{span}\{|0; 1\rangle_L, |11; 00\rangle\}, \\ \mathcal{H}_3 &= \text{span}\{|1; 0\rangle_L, |00; 11\rangle\}, \\ \mathcal{H}_4 &= \text{span}\{|1; 1\rangle_L, |02; 00\rangle, |00; 02\rangle\}. \end{aligned} \tag{28}$$

We have ensured that the evolution acts as an identity on the first three subspaces (\mathcal{H}_1 to \mathcal{H}_3). The derivation within the fourth subspace, responsible for generating the CPhase gate, is more involved; interested readers are referred to Section II of the Supplementary Note for a detailed treatment.

Here, we summarize the key constraints and the accumulated phase. The requirement that the state remains in the logical subspace at T_{CP}

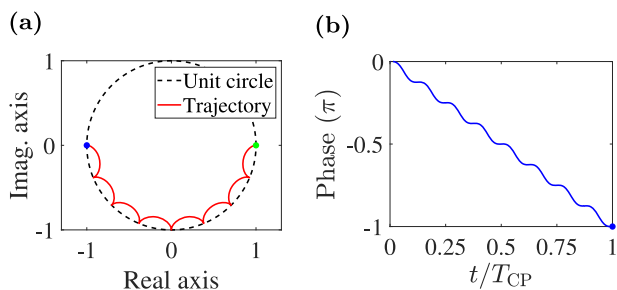


Fig. 3 | Evolution of the state $|1; 1\rangle_L$ for implementing a CZ gate. a Coefficient trajectory (solid red line) of $|1; 1\rangle_L$ in the complex plane. The black dashed curve shows the unit circle. The x -axis and y -axis represent the real and imaginary parts, respectively. The state starts at $(1, 0)$ (green dot) and ends at the target point $(-1, 0)$ (blue dot). **b** Phase evolution. The phase decreases continuously with small oscillations, reaching $-\pi$ at the gate time.

imposes the following condition on the system parameters:

$$\frac{U - V_{CP}}{J_{CP}} = \pm \sqrt{m^2 - 16}, \quad m \in \mathbb{N}, m \geq 4. \quad (29)$$

Under this constraint, the accumulated phase at T_{CP} is given by

$$\varphi_m = -\pi \left(\frac{2V_{CP}}{J_{CP}} - \sqrt{m^2 - 16} - m \right). \quad (30)$$

Thus, the unitary evolution operator $\hat{U}_{CP}(T_{CP})$ can be expressed as a block diagonal matrix, with contributions from the logical subspace and the orthogonal subspace \mathcal{H}_\perp :

$$\hat{U}_{CP}(T_{CP}) = \hat{U}_{CP} \oplus \hat{U}_\perp = \text{diag}(1, 1, 1, \exp(i\varphi_m)) \oplus \hat{U}_\perp, \quad (31)$$

where \hat{U}_\perp acts on \mathcal{H}_\perp , the non-logical subspace. For integers $m \geq 4$, the desired phase φ_m can be achieved by selecting an appropriate value for m and tuning the ratio V_{CP}/J_{CP} .

Next, we apply this framework to a practical parameter set for the CZ gate. Typically, the effective ZZ strength V_{CP} is much smaller than the coupling strength J_{CP} . We choose $m = 8$, leading to a ratio $V_{CP}/J_{CP} \approx -0.036$. Under this condition, the restriction in Eq. (29) simplifies to:

$$U = V_{CP} \pm 4\sqrt{3}J_{CP}. \quad (32)$$

Since the anharmonicity of a transmon is negative, we select the minus sign, yielding $U \approx -6.964J_{CP}$. We adopt J_{CP} as the unit of energy, and for a typical coupling strength $J_{CP}/2\pi = 40$ MHz, we estimate:

$$V_{CP}/2\pi \approx -1.44 \text{ MHz}, \quad U/2\pi \approx -278.6 \text{ MHz}. \quad (33)$$

These values lie within the practical regime for the transmon and tunable coupling scheme, corresponding to a gate time of $T_{CP} = 25$ ns.

The small ratio V_{CP}/J_{CP} can be increased by employing an alternative coupling scheme, as proposed in ref. 34, where the coupler consists of a parallel combination of a capacitor and a Josephson junction, potentially allowing for V/J ratios greater than one.

We show the population evolution for the CZ gate in Fig. 2(b), using parameters $m = 8$, $V_{CP} = (-7/2 + 2\sqrt{3})J_{CP}$, and $U = -(7/2 + 2\sqrt{3})J_{CP}$. The initial states are chosen from the logical subspace \mathcal{H}_L , with $|\psi(0)\rangle = |0; 1\rangle_L$ in Fig. 2(b1) or $|1; 1\rangle_L$ in Fig. 2(b2). The population of each logical basis state returns to unity at the gate time T_{CP} , and the population of $|1; 1\rangle_L$ remains large throughout the evolution, maximizing the effect of the ZZ interaction.

We further present the numerical evolution of the basis state $|1; 1\rangle_L$ in Fig. 3. It evolves under the Hamiltonian H_4 . In Fig. 3(a), we show the

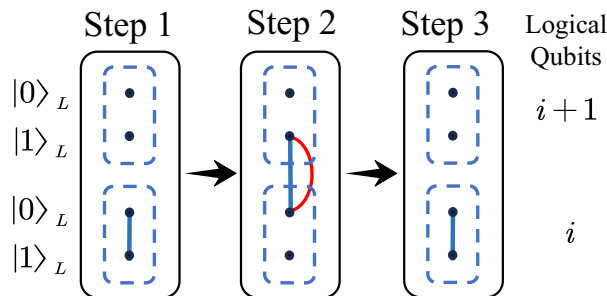


Fig. 4 | Implementation of the CPhase gate with longitudinally connected logical qubits. Since the coupling between logical qubits is restricted to $|0_i\rangle_L$ and $|1_{i+1}\rangle_L$, a basis transformation is required to swap $|0_i\rangle_L$ into $|1_i\rangle_L$. We first perform an X gate on the i -th logical qubit. The second step follows the same procedure as outlined in the previous subsection. Finally, another X gate is applied to revert the basis back to its original form.

trajectory of the complex coefficient of $|1; 1\rangle_L$. Initialized at $(x = 1, y = 0)$ (green dot), the state evolves into the target point $(-1, 0)$ (blue dot) at the gate time T_{CP} , corresponding to $|\psi(T_{CP})\rangle = -|1; 1\rangle_L$. Figure 3(b) illustrates the phase accumulation of the coefficient of $|1; 1\rangle_L$, which decreases with small oscillations, reaching $-\pi$ at the gate time.

In conclusion, both analytical calculations and numerical simulations verify that the logical basis states return to themselves, while the state $|1; 1\rangle_L$ acquires an additional phase of $-\pi$, confirming the successful implementation of the CZ gate.

CPhase gate for longitudinal connections

As shown in Fig. 1(a), longitudinally connected logical qubits are restricted to a single coupling between sites $(i, 0)$ and $(i + 1, 1)$, limiting the available two-qubit gate operations. However, similar to the transverse connection, the CPhase gate can still be implemented by utilizing a single coupling, with additional single-qubit operations. This process is illustrated in Fig. 4.

The implementation proceeds in three steps. First, a local X-gate is applied to the i -th logical qubit, transforming $|1_i\rangle_L$ into $|0_i\rangle_L$. This operation takes a time $t_1 = \pi/(2J_X)$, where J_X is the coupling strength for the X-gate. The second step involves applying a CPhase operation, following the procedure from the previous subsection, with a duration $t_2 = 2\pi/|J_{CP}|$, where J_{CP} is the coupling strength for the CPhase gate. After this step, the state $|0_i 1_{i+1}\rangle_L$ acquires an additional phase. Finally, a second X-gate is applied to return the basis state to its original form, taking a time $t_3 = t_1$.

Thus, the total gate time for the longitudinal CPhase gate is:

$$T_{CPL} = \pi \left(\frac{1}{J_X} + \frac{2}{J_{CP}} \right). \quad (34)$$

It is important to note that the coupling strengths vary for different operations. The X-gate demands a zero ZZ interaction strength $V_X = 0$, while the CPhase gate requires a specific ratio between V_{CP} and J_{CP} to ensure the correct phase accumulation.

iSWAP gate for transverse connections

The iSWAP gate is another maximally entangling gate and, when combined with single-qubit gates, forms a universal gate set for quantum computation⁴³. In the transverse connection mode, the iSWAP gate can readily be implemented using the ZZ interaction. To achieve this, we consider implementing an iSWAP operation with a global phase i , denoted by \hat{U}_S , whose matrix representation is:

$$\hat{U}_S = i \cdot \hat{U}_{i\text{SWAP}} = i \begin{pmatrix} 1 & 0 & 0 & 0 \\ 0 & 0 & i & 0 \\ 0 & i & 0 & 0 \\ 0 & 0 & 0 & 1 \end{pmatrix} = \begin{pmatrix} i & 0 & 0 & 0 \\ 0 & 0 & -1 & 0 \\ 0 & -1 & 0 & 0 \\ 0 & 0 & 0 & i \end{pmatrix}. \quad (35)$$

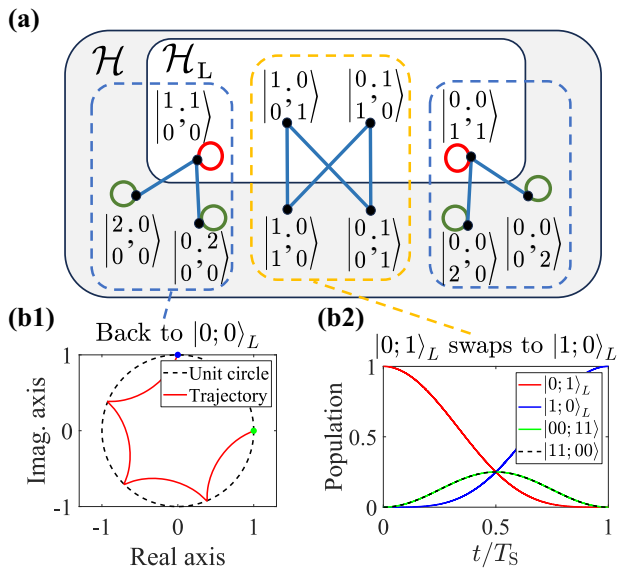


Fig. 5 | Dual graph and evolution of the iSWAP Gate on dual-rail encoded qubits. **a** The graph illustrates the couplings and interactions between Fock states under the Hamiltonian \hat{H}_S . It consists of 10 vertices, each representing a basis state in the Fock space \mathcal{H} of two bosons distributed over four sites. The four selected states span the logical subspace \mathcal{H}_L . Blue edges correspond to allowed couplings, red self-loops represent ZZ interactions, and green self-loops correspond to on-site interactions. **b1** Coefficient trajectory of the state $|0; 0\rangle_L$ on the complex plane. The state begins at $(1, 0)$ (green dot) and evolves to $(0, 1)$ (blue dot) at the gate time T_S . At the final time, the population of $|0; 0\rangle_L$ is unity, and the accumulated phase is i . **b2** Evolution of the state $|0; 1\rangle_L$ swapping to $|1; 0\rangle_L$. The x-axis shows the evolution time in units of T_S , while the y-axis indicates the population of the involved states. Despite the non-logical states being populated during the evolution, their populations diminish by the time T_S , confirming a perfect swap process.

A straightforward implementation of this gate involves simultaneously opening the couplings between adjacent logical qubits $|x_i\rangle_L$ and $|x_{i+1}\rangle_L$ for each $x \in \{0, 1\}$, as shown in Fig. 1(b). The additional global phase i is compensated by applying a frequency shift $\mu_S \hat{n}$ to each of the four physical qubits until their phase accumulations reach $-\pi/2$.

For simplicity, we focus on the \hat{U}_S operation. Denoting the coupling and interaction strengths as J_S and V_S , the system Hamiltonian is:

$$\hat{H}_S = -J_S(\hat{c}_{i,0}^\dagger \hat{c}_{i+1,0} + \hat{c}_{i,1}^\dagger \hat{c}_{i+1,1} + \text{H.c.}) + V_{CP}(\hat{n}_{i,0} \hat{n}_{i+1,0} + \hat{n}_{i,1} \hat{n}_{i+1,1}) + \hat{H}_0, \quad (36)$$

where \hat{H}_0 is the default Hamiltonian. The evolution operator is $\hat{U}_S(t) = \exp(-i\hat{H}_S t)$. As in previous subsections, we derive conditions for unitary evolution within the logical subspace \mathcal{H}_L and examine the system's action on the logical basis states, as shown in Fig. 5(a). The dashed boxes can be classified into two scenarios, marked by orange or blue colors.

In the first scenario, the Hamiltonian \hat{H}_S couples the logical states $|10; 01\rangle$ and $|01; 10\rangle$, along with non-logical states $|11; 00\rangle$ and $|00; 11\rangle$. Their dynamics are governed by two simultaneous Rabi oscillations. Assuming an initial state $|10; 01\rangle$, the evolutions for the upper and lower rows are, respectively:

$$\begin{aligned} \hat{U}_S(t)|10\rangle &= \cos(J_S t)|10\rangle + i \sin(J_S t)|01\rangle, \\ \hat{U}_S(t)|01\rangle &= \cos(J_S t)|01\rangle + i \sin(J_S t)|10\rangle. \end{aligned} \quad (37)$$

Thus, the evolution of the two-qubit state $|10; 01\rangle$ becomes:

$$\hat{U}_S(t)|10; 01\rangle = \cos^2(J_S t)|10; 01\rangle - \sin^2(J_S t)|01; 10\rangle + \frac{i}{2} \sin(2J_S t)(|11; 00\rangle + |00; 11\rangle). \quad (38)$$

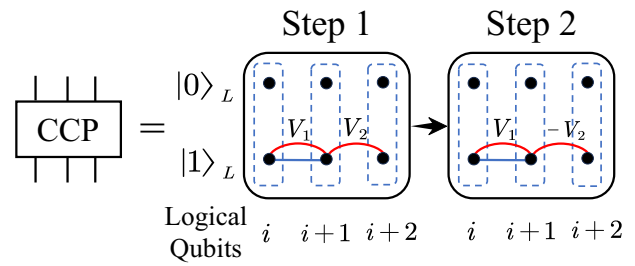


Fig. 6 | Implementation of the CCPhase Gate with three neighboring logical qubits. The gate operation consists of two steps. In each step, a CZ gate is applied to the first two qubits in the $x = 1$ row while alternately enabling ZZ interactions V_2 and $-V_2$ between the latter two qubits. This ensures zero phase accumulation for $|1; 1; 0\rangle_L, |1; 0; 1\rangle_L$, and $|0; 1; 1\rangle_L$, while a nonzero phase is accumulated exclusively on $|1; 1; 1\rangle_L$.

To achieve a perfect swap of the logical states $|10; 01\rangle$ and $|01; 10\rangle$, the gate time must satisfy:

$$T_S = \frac{(2k + 1)\pi}{2J_S}, \quad k \in \mathbb{N}. \quad (39)$$

At this time, the evolution is:

$$\hat{U}_S(T_S)|10; 01\rangle = -|01; 10\rangle, \quad \hat{U}_S(T_S)|01; 10\rangle = -|10; 01\rangle. \quad (40)$$

Due to the symmetry of \hat{H}_S , the evolutions and restrictions for the state $|01; 10\rangle$ are identical.

In the second scenario, the evolution of the states $|10; 10\rangle$ and $|01; 01\rangle$ proceeds similarly to that described in Section II of the Supplementary Note, differing only in the gate time. We defer the detailed restrictions to Section III of the Supplementary Note and present here a viable set of system parameters:

$$V_S \approx 0.1 J_S, \quad U \approx -3.4 J_S, \quad (41)$$

which corresponds to a total iSWAP gate time of

$$T_S = \frac{5\pi}{2J_S}. \quad (42)$$

Within this interval, the detuning on each physical qubit is set to $\mu_S = -0.2 J_S$ to ensure the accumulation of a global phase of $-i$.

In Fig. 5(b), we show the numerical evolution of the basis states during the iSWAP gate operation with the parameters described above. In Fig. 5(b1), we present the trajectory of the complex coefficient for $|0; 0\rangle_L$ (equivalently $|1; 1\rangle_L$). Starting with $|\psi(0)\rangle = c(0)|0; 0\rangle_L$ and $c(0) = 1$ (green dot), the evolution leads back to $|0; 0\rangle_L$ at T_S , with $c(T_S) = i$ (blue dot), completing the desired operation. In Fig. 5(b2), we show the swapping dynamics between $|0; 1\rangle_L$ and $|1; 0\rangle_L$. The x-axis represents the evolution time, and the y-axis indicates the population of the involved states. The populations follow $\cos^4(J_S t)$ and $\sin^4(J_S t)$ curves during the evolution, demonstrating smooth transitions between the two states. This suggests potential robustness against fluctuations in the coupling strength J_S , which could be advantageous for practical implementations.

CCPhase gate for transverse connections

The CCPhase gate is a crucial operation for three neighboring logical qubits, requiring precise control of phase accumulation across logical basis states. This subsection introduces the implementation of the CCPhase gate using a two-step approach, ensuring phase cancellation for all states except $|1; 1; 1\rangle_L$, which accumulates the desired phase shift.

We illustrate the quantum walk dynamic diagram for implementing the CPhase gate in Fig. 6. In each step, a CZ gate is applied to the first two qubits in the $x = 1$ row while alternately enabling ZZ interactions V_2 and $-V_2$ between the latter two qubits.

The dynamics are confined to states involving at least one walker in the $x = 1$ row. For states with one walker in the $x = 1$ row ($|1; 0; 0\rangle_L$, $|0; 1; 0\rangle_L$, and $|0; 0; 1\rangle_L$), the Rabi oscillation between the first two states requires a time identical to T_{CP} , while the last state is stationary. Thus, the two-step approach sets up the gate time $T_{CCP} = 2T_{CP}$.

There are three two-walker states, $|1; 0; 1\rangle_L$, $|0; 1; 1\rangle_L$, and $|1; 1; 0\rangle_L$. The first two states are coupled due to the coupling between $|1_i\rangle_L$ and $|1_{i+1}\rangle_L$, while the dynamics of the third state are the same as in CPhase gate.

The Hamiltonian acting on the states $|1; 0; 1\rangle_L$ and $|0; 1; 1\rangle_L$ is described as

$$\hat{H}_1 = \begin{pmatrix} 0 & -J \\ -J & V_2 \end{pmatrix}. \tag{43}$$

The eigenvalues and eigenstates are:

$$\begin{aligned} \lambda_{1,2} &= \frac{1}{2} \left(V_2 \pm \sqrt{4J^2 + V_2^2} \right), \\ |\phi_{1,2}\rangle &= \alpha_{1,2} \left(\frac{V_2 \pm \sqrt{4J^2 + V_2^2}}{2J}, 1 \right)^T. \end{aligned} \tag{44}$$

To ensure $|1; 0; 1\rangle_L$ and $|0; 1; 1\rangle_L$ return to their original states after T_{CP} , the interaction strength must satisfy:

$$\frac{V_2}{J} = \pm \sqrt{k^2 - 4}, \quad k \geq 2, \quad k \in \mathbb{N}. \tag{45}$$

Under this restriction, the accumulated phase on $|1; 0; 1\rangle_L$ reads

$$\varphi_{101}(V_2) = -\pi \left(\frac{V_2}{J} + k \right). \tag{46}$$

Thus, the phase accumulation cancels over two steps:

$$\varphi_{101}(V_2) + \varphi_{101}(-V_2) = 0. \tag{47}$$

These arguments apply to the state $|0; 1; 1\rangle_L$ as well.

On the other hand, the dynamics of $|1; 1; 0\rangle_L$ mimic those of $|1; 1\rangle_L$ in the CPhase gate. To prevent leakage, the condition is:

$$\frac{U - V_1}{J} = \pm \sqrt{m^2 - 16}, \quad m \geq 4, \quad m \in \mathbb{Z}. \tag{48}$$

Zero accumulated phase requires:

$$\frac{V_1}{J} = \frac{1}{2} (\sqrt{m^2 - 16} + m + k), \quad k \in \mathbb{Z}. \tag{49}$$

Finally, for three walkers, $|1; 1; 1\rangle_L$ couples to non-logical states $|2; 0; 1\rangle_L$ and $|0; 2; 1\rangle_L$, described by the Hamiltonian:

$$\hat{H}_2 = \begin{pmatrix} V_1 + V_2 & -\sqrt{2}J & -\sqrt{2}J \\ -\sqrt{2}J & U & 0 \\ -\sqrt{2}J & 0 & U + 2V_2 \end{pmatrix}. \tag{50}$$

For small V_2/J , we find the resulting phase accumulation is negligibly small by applying perturbative calculations. When V_2/J is large, we can search possible parameters to ensure $|1; 1; 1\rangle_L$ return to itself after T_{CP} , while V_2 being around the value given in Eq. (45).

If setting $k = 5$, the parameters achieving fidelity $F \geq 0.99$ are:

$$\begin{aligned} \frac{V_2}{J} &\approx \sqrt{21}, \quad m \geq 17, \quad \frac{V_1}{J} \approx 0.25, \\ U &= V_1 - \sqrt{m^2 - 16}. \end{aligned} \tag{51}$$

The large values of V_1 and V_2 require a different coupling scheme as proposed in ref. 34. We find that the maximum phase on $|1; 1; 1\rangle_L$ is -0.078π , as shown in Section IV of the Supplementary Note. The total gate time is $T_{CCP} = 2T_{CP}$.

Noise analysis on the CZ gate

In this subsection, we analyze the effects of various noise sources on the performance of the CZ gate in superconducting circuits. The CZ gate serves as a representative example due to its practical implementation within a single step under realistic parameters. The primary noise sources considered are:

- **Dephasing.** Fluctuations in qubit energy levels lead to loss of coherence and degrade gate fidelity.
- **Relaxation.** Energy relaxation from the excited to the ground state during gate operation reduces the population of the logical subspace, introducing errors.
- **Inaccurate Hamiltonian parameters.** Deviations in coupling strength J and interaction strength V can cause the system's evolution to diverge from the ideal unitary operation.
- **Detuning errors.** Misalignment in detuning between adjacent logical qubit sites affects phase accumulation, potentially inducing leakage into non-logical subspaces.

Strategies to mitigate these effects include parameter optimization, error correction, and noise-resilient designs for superconducting circuits. We will quantify the impact of these noise sources on the CZ gate. The Hamiltonian parameters for the CZ gate implementation are set as follows: $m = 8$, $V_{CP} = (-7/2 + 2\sqrt{3})J_{CP}$, $U = -(7/2 + 2\sqrt{3})J_{CP}$, and $\mu = 0$.

In the following, we focus on dephasing and relaxation. The representation of Fock states permits the modeling of decoherence utilizing methodologies analogous to those employed for individual transmons. This is in contrast to the scenario described in ref. 5, where the utilization of dressed states within the encoded logical basis modifies the decoherence rates. To explain the main noise mechanisms, dephasing and relaxation, we use the standard Lindblad-form Markovian master equation.

$$\frac{d\rho}{dt} = -\frac{i}{\hbar} [\hat{H}, \rho] + \sum_k \left(\hat{L}_k \rho \hat{L}_k^\dagger - \frac{1}{2} \{ \hat{L}_k^\dagger \hat{L}_k, \rho \} \right), \tag{52}$$

where ρ is the density matrix of the system, \hat{H} is the system Hamiltonian, and \hat{L}_k are the Lindblad operators that describe the interaction between the system and its environment. This framework, which is widely used for modeling decoherence in transmon systems (see, e.g., ref. 44), allows us to efficiently analyze the impact of environmental noise on our logical qubits.

Dephasing noise leads to coherence loss without altering population distributions in the logical basis. For a homogeneous dephasing rate γ , the Lindblad operator associated with each logical basis state $|k\rangle$ is:

$$\hat{L}_k = \sqrt{\gamma} |k\rangle \langle k|. \tag{53}$$

Relaxation involves energy dissipation and is characterized by the relaxation rate Γ . The Lindblad operators for relaxation on each physical qubit are given by:

$$\hat{L}_{\downarrow,ix} = \sqrt{\Gamma} \sum_{k=0,1} |k\rangle \langle k+1|, \tag{54}$$

where i and x index the qubit in a $2 \times n$ array of physical qubits.

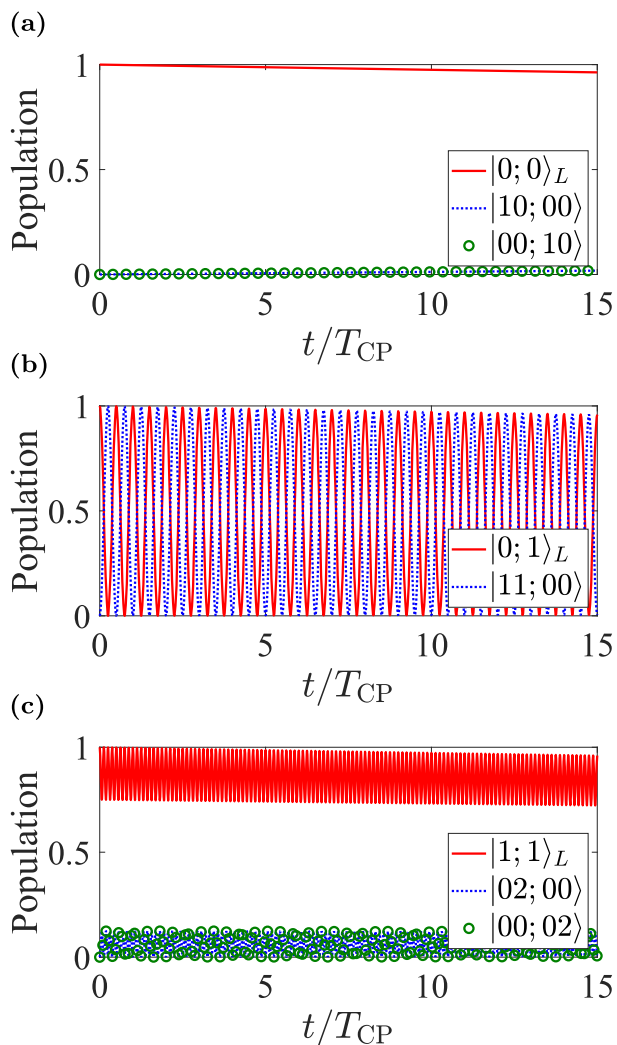


Fig. 7 | Population dynamics of basis states under relaxation and dephasing Noise. The logical basis states are represented by the red lines. **a** The population of the state $|0; 0\rangle_L$ decreases due to relaxation, while the populations of the leakage states $|10; 00\rangle$ (blue dashed) and $|00; 10\rangle$ (green circle) increase. **b** The population of the logical state $|0; 1\rangle_L$ decreases, accompanied by a decay in the leakage state $|11; 00\rangle$ (blue dashed). **c** The population of the logical state $|1; 1\rangle_L$ decreases due to relaxation, whereas the leakage states $|02; 00\rangle$ (blue dashed) and $|00; 02\rangle$ (green circle) show negligible decay.

We use a state-of-the-art relaxation time $T_1 = 100 \mu\text{s}^1$, corresponding to $\Gamma = J/5000$ when the coupling strength $J/2\pi = 50 \text{ MHz}$. The dephasing rate is set to $\gamma = \Gamma$, consistent with typical experimental conditions. Notably, dual-rail qubits encoded in resonantly coupled transmons have demonstrated coherence times exceeding milliseconds⁵, highlighting their potential for quantum information processing.

The numerical simulation results are presented in Fig. 7, showcasing the effects of dephasing and relaxation noise on the population dynamics of selected initial states: $|0; 0\rangle_L$, $|0; 1\rangle_L$, and $|1; 1\rangle_L$. The simulations were performed using the `ode45` solver in MATLAB to solve the Lindblad master equation, with the evolution time extending up to 15 times the CPhase gate duration.

In Fig. 7(a), the initial state $|0; 0\rangle_L$ experiences a population decay to 0.963 by the end of the evolution, accompanied by a population growth in the leakage states $|10; 00\rangle$ and $|00; 10\rangle$, which together account for 0.037 of the total population. These leakage events, which can be detected and converted into erasure errors, highlight the importance of error mitigation strategies.

Figure 7 (b) shows the evolution of the state $|0; 1\rangle_L$, which exhibits Rabi oscillations with the leakage state $|11; 00\rangle$. By the end of the evolution, the population of $|0; 1\rangle_L$ decreases to 0.959, while the leakage states $|10; 00\rangle$ and $|00; 01\rangle$ acquire populations of 0.0183 and 0.0137, respectively. This behavior underscores the need for an effective error correction scheme tailored to this subspace.

Finally, Fig. 7(c) examines the dynamics of the initial state $|1; 1\rangle_L$, which decays to a population of 0.960. The associated leakage states $|02; 00\rangle$ and $|00; 02\rangle$, critical for phase accumulation, exhibit negligible population changes, with their combined population decreasing marginally from 0.125 to 0.121. The remaining population loss is primarily accounted for by the leakage states $|00; 01\rangle$ and $|01; 00\rangle$, which together contribute 0.035. These results suggest that the phase deviation introduced by the leakage states $|02; 00\rangle$ and $|00; 02\rangle$ is minor, maintaining the robustness of the phase-sensitive operations.

We next analyze parameter deviations on the CZ gate. Understanding the robustness of the CZ gate to parameter deviations is crucial for reliable quantum computation. Variations in the coupling strength J and interaction strength V , caused by flux noise or crosstalk, can alter the effective Hamiltonian and introduce leakage or fidelity loss. This section examines the impact of such deviations and quantifies their effects on gate performance, including leakage and fidelity.

The coupler frequency determines both J and V , making the system sensitive to flux noise. Additionally, crosstalk can induce residual ZZ interactions⁴⁵. Typical deviations in superconducting circuits include shifts in the coupling strength of approximately $5 \text{ kHz} \times 2\pi$ and residual ZZ interactions up to $10 \text{ kHz} \times 2\pi$. These deviations can prevent the system from fully returning to the logical subspace at the end of the gate operation, leading to true leakage events.

The fidelity of the CZ gate is defined using the expression⁴⁶:

$$F = \frac{1}{n(n+1)} [\text{Tr}(MM^\dagger) + |\text{Tr}(M)|^2], \quad (55)$$

where n is the dimension of the logical subspace, $M = PU_{CZ}^\dagger UP$, and $U_{CZ} = \text{diag}(1, 1, 1, -1)$ is the ideal CZ gate unitary. Here, U is the unitary operation under noise, and P projects onto the logical subspace \mathcal{H}_L . This formula is particularly useful in quantum information theory for assessing the performance of quantum operations, especially in the presence of imperfections or noise. It allows for the quantification of how closely an implemented operation approximates the intended operation, averaged over all possible input states. The first term in F quantifies leakage, while the second term measures the deviation from the ideal operation.

Figure 8 illustrates the effects of deviations in J and V on the fidelity and leakage of the CZ gate. The x -axis represents variations in J (in units of J_{CP}), and the y -axis shows deviations in V (in units of $|V_{CP}|$). The left panels present a broad deviation range, highlighting uncontrollable behaviors for large parameter variations. The right panels focus on a narrower region around the optimal values $J = J_{CP}$ and $V = V_{CP}$, corresponding to realistic noise levels in superconducting circuits.

For a typical coupling strength $J/2\pi = 40 \text{ MHz}$, deviations of $\delta J/2\pi = 0.01J/2\pi \approx 0.4 \text{ MHz}$ and $\delta V/2\pi \approx 0.4 \text{ MHz}$ well capture realistic experimental noise. Due to the large value of U , rapid phase accumulation by the states $|00; 20\rangle$ and $|00; 02\rangle$ significantly contributes to the $-\pi$ phase, while contributions from ZZ interaction is much weaker. Consequently, deviations in J have a greater impact on gate fidelity than those in V . Leakage is even more sensitive to J , as deviations hinder the return to the logical subspace.

In conclusion, implementing the two-qubit CZ gate is feasible when considering the parameter deviations present in superconducting circuits.

Another relevant error mechanism arises from the detuning of neighboring transmons. Superconducting qubits often exhibit inhomogeneities due to fabrication precision limitations. One significant source of

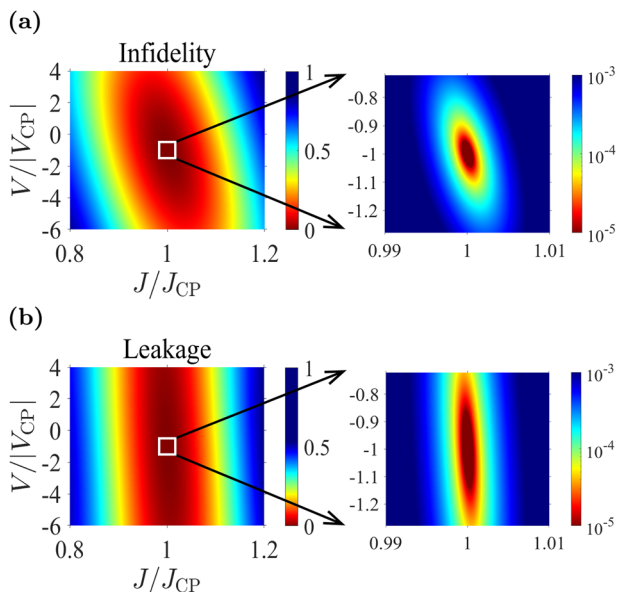


Fig. 8 | Impact of parameter imperfections on CZ gate performance. The results are shown via (a) fidelity and (b) leakage. The x-axis represents deviations in the coupling strength, measured in units of J_{CP} , while the y-axis corresponds to the ZZ interaction strength, expressed in units of $|V_{CP}|$. The right panels provide a magnified view of the region near the optimal parameters $J = J_{CP}$ and $V = V_{CP}$. Owing to the large value of U , variations in J have a more pronounced effect compared to deviations in V . Nevertheless, the impact of both parameters remains within acceptable bounds under typical experimental noise conditions.

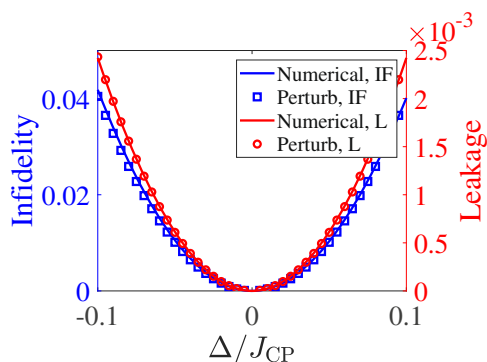


Fig. 9 | Performance of the CZ gate under detuning noise. The x-axis represents the detuning strength Δ , expressed in units of J_{CP} . The left and right y-axes correspond to the CZ gate’s infidelity and leakage, respectively. The solid lines depict the results from exact numerical simulations, while the squares and circles represent the second-order perturbation theory. The close agreement between the exact and perturbation results confirms a quadratic dependence of both infidelity and leakage on Δ .

errors in gate operations is detuning between adjacent qubits. This subsection explores the impact of detuning on the implementation of a CZ gate between the i -th and $i + 1$ -th logical qubits, particularly focusing on the influence of detuning noise between the second rows of the two columns. The detuning is defined as:

$$\Delta \equiv \mu_{i+1,1} - \mu_{i,1}. \tag{56}$$

This leads to a modified Hamiltonian:

$$\hat{H}_{CP,detuned} = \hat{H}_{CP} + \Delta \hat{n}_{i+1,1}. \tag{57}$$

Due to the detuning, we expect imperfect evolution, resulting in leakage from the logical subspace. Specifically, the final state may have nonzero support in the orthogonal subspace, and we quantify the gate performance by examining both fidelity and leakage.

Given that the relevant subspaces are of dimension 2 or 3, we can analytically compute the average gate fidelity under detuning noise without additional assumptions. For simplicity, we assume a small detuning Δ , such that $\Delta/J \ll 1$, and investigate the fidelity dependence on Δ .

We begin by recalling the four subspaces from Eq. (28) and analyze each subspace in turn. The action of $\hat{H}_{CP,detuned}$ in the space \mathcal{H}_1 remains unchanged, identical to that of \hat{H}_{CP} .

In \mathcal{H}_2 , the modified Hamiltonian is:

$$\hat{H}'_2 = \begin{pmatrix} \Delta & -J \\ -J & 0 \end{pmatrix}. \tag{58}$$

The eigenvalues are:

$$\lambda_{\pm} = \frac{\Delta \pm \sqrt{\Delta^2 + 4J^2}}{2}, \tag{59}$$

and the corresponding eigenstates are:

$$|\phi_{\pm}\rangle = \alpha_{\pm} \begin{pmatrix} \lambda_{\pm}/J \\ -1 \end{pmatrix}, \tag{60}$$

where $\alpha_{\pm} = 1/\sqrt{1 + \lambda_{\pm}^2/J^2}$ are normalization coefficients. The state $|0; 1\rangle_L$ should be invariant under the perfect operation \hat{U}_{CZ} . Initializing the state $|0; 1\rangle_L$ and evolving it under H'_2 , the coefficient of $|0; 1\rangle_L$ at the gate time T_{CP} becomes:

$$c_2 = \left(\frac{\alpha_+ \lambda_+}{J}\right)^2 e^{-i\lambda_+ T_{CP}} + \left(\frac{\alpha_- \lambda_-}{J}\right)^2 e^{-i\lambda_- T_{CP}}. \tag{61}$$

Assuming a small $\delta = \Delta/J$, we obtain $c_2 \approx e^{-i\pi\delta}$.

In \mathcal{H}_3 , the Hamiltonian is:

$$\hat{H}'_3 = \begin{pmatrix} 0 & -J \\ -J & \Delta \end{pmatrix}, \tag{62}$$

which is related to \hat{H}'_2 by a basis permutation. The coefficient of the logical state $|10\rangle_L$ is:

$$c_3 = \alpha_+^2 e^{-i\lambda_+ T_{CP}} + \alpha_-^2 e^{-i\lambda_- T_{CP}}, \tag{63}$$

which simplifies to $c_3 \approx e^{-i\pi\delta}$.

Finally, in \mathcal{H}_4 , after extensive derivations (see Section V of the Supplementary Note for details), the coefficient for the state $|11\rangle_L$ at the gate time is given by

$$c_4 \approx -\left(1 + \frac{\delta^2}{4} e^{i4\sqrt{3}\pi}\right) e^{-2\pi i\delta}. \tag{64}$$

The projected matrix is $PUP = \text{diag}(1, c_2, c_3, c_4)$. The fidelity $F(\Delta)$ and leakage $L(\Delta)$ are:

$$\begin{aligned} F(\Delta) &= 1 + \frac{\cos(4\sqrt{3}\pi)\delta^2}{10} - \frac{2\pi^2\delta^2}{5}, \\ L(\Delta) &= -\frac{\cos(4\sqrt{3}\pi)\delta^2}{16}. \end{aligned} \tag{65}$$

The quadratic dependence of fidelity and leakage on Δ demonstrates the robustness of the CZ gate against detuning noise. For a typical detuning of $\Delta/2\pi = 0.1$ MHz and $J/2\pi = 40$ MHz, we obtain $\delta = 0.0025$, leading to an

infidelity of approximately 2.5×10^{-5} , confirming the applicability of the CZ gate under detuning noise.

Numerical results in Fig. 9 validate the quadratic dependence of fidelity and leakage on Δ , in good agreement with the perturbation analysis.

Circuit example: preparation of a GHZ state

The Greenberger-Horne-Zeilinger (GHZ) state is a highly entangled quantum state involving multiple qubits and is an essential example of multi-qubit entanglement. For three qubits, the GHZ state is expressed as

$$|\text{GHZ}\rangle = \frac{1}{\sqrt{2}}(|000\rangle + |111\rangle). \tag{66}$$

The preparation and manipulation of GHZ states are important benchmarks for quantum hardware performance and are crucial for the development of scalable quantum technologies.

As shown in Fig. 10, a 3-qubit GHZ state can be efficiently prepared using dual-rail encoded qubits. Figure 10(a) presents the logic circuit for generating the state, which involves a Hadamard gate on Q_2 , followed by two CNOT gates, one between Q_1 and Q_2 , and another between Q_2 and Q_3 . Figure 10(b) shows the corresponding quantum walk graphs at each step. The preparation process requires two Hadamard gates and one CZ gate to implement the CNOT gate. Notably, single-qubit gates can be applied simultaneously on different logic qubits. In total, the GHZ state can be prepared in five steps for dual-rail encoded qubits: the first step involves a Hadamard gate on Q_2 , followed by the implementation of the CNOT gate between Q_1 and Q_2 from steps 1 to 3, and the final CNOT gate between Q_2 and Q_3 from steps 3 to 5.

Discussion

The following key points merit further discussion regarding this framework:

- Bosons hopping on a lattice described by the extended Bose-Hubbard model can be interpreted as multiple quantum walkers on a graph whose vertices and edges encode the sites and couplings, respectively. Multiple walkers on $2 \times n$ vertices provide exponentially growing resources to accommodate dual-rail encoding, establishing a scalable architectural framework for quantum computation. After introducing a controlled ZZ interaction, this model enables the implementation of maximally entangling gates and a universal gate set for dual-rail encoded qubits.
- This system enables perfect adiabatic control and leverages the ability to access the non-logical subspace during evolution while being entirely confined to the logical subspace by the end of the evolution. Therefore, our photon-number-conserving gate operations maintain the parity structure of the dual-rail encoding, ensuring that when relaxation errors or leakage errors occur, they remain detectable with established measurement protocols for dual-rail encoded qubits⁵⁻⁷. This integration of control operations with existing measurement schemes provides a complete pathway to error-detectable quantum computation without requiring new measurement techniques—a significant advancement toward fault tolerance.
- On the 2-dimensional dual-rail encoded qubit array, we demonstrate schemes for implementing single-qubit gates, two-qubit CPhase and iSWAP gates, and a three-qubit CCPhase gate in transverse connections, along with a CPhase gate in longitudinal connections. Using parameters compatible with current tunable coupling schemes in superconducting circuits, two-qubit gates achieve theoretical fidelity of unity, while the CCPhase gate demonstrates phases up to -0.078π with fidelity ≥ 0.99 . Our numerical and analytical analyses confirm robust performance against dephasing, relaxation, coupling imperfections, and ZZ interaction variations, with the CZ gate exhibiting first-order insensitivity to inter-qubit detuning.
- Our proposed architecture is hardware-efficient because it requires fewer hardware modifications, lower resource costs, and straightforward integration with today’s superconducting qubit technologies.

Specifically: 1. It aligns with existing transmon and tunable coupler designs. Dual-rail encoding can be realized by pairs of transmons and a flux-tunable coupler, both of which are standard elements in many superconducting quantum devices. 2. It avoids reliance on large numbers of ancillary qubits or intricate multi-level control schemes. By encoding a single photon-number excitation across two transmons and employing CTQW, the architecture stays relatively simple and utilizes hardware components that are already typical in current experiments. 3. It naturally converts leakage and relaxation into erasure events, simplifying error detection and correction rather than requiring extra measurement circuitry or feedback control and correction.

- While our analysis focuses on superconducting circuits, the framework is extensible to other physical platforms supporting coherent bosonic excitations and controllable interactions, including neutral atoms in optical lattices, trapped ions, or photonic waveguide arrays, as experimentally demonstrated with both transmons and superconducting cavities.

In conclusion, we have demonstrated how combining dual-rail qubit encoding with continuous-time quantum walks in superconducting architectures offers a hardware-efficient route toward robust and scalable quantum computation. We harnessed photon-number-conserving dynamics to suppress population leakage and enable high-fidelity single-, two-, and three-qubit gate operations, thereby matching the goal of dual-rail encoded qubits to convert erasure errors. Our theoretical and numerical results indicate that this synergy not only mitigates conventional sources of decoherence (e.g., dephasing and relaxation) but also remains tolerant to coupling imperfections, underscoring the resilience of the dual-rail framework.

Beyond the immediate gains in gate fidelity and error correction, this approach can serve as a foundation for early fault-tolerant quantum computing. Since erasure errors are more tractable in quantum error-correcting codes, adopting a dual-rail strategy may simplify the overhead associated with representative fault-tolerant protocols. Moreover, by exploiting tunable coupler strengths—already feasible in present-day superconducting devices—our method aligns well with current experimental capabilities, paving the way for near-term demonstrations of larger-scale quantum systems.

Methods

Transmons connected with tunable couplers

We begin with a 2-D superconducting circuit consisting of transmons and tunable couplers, as depicted in Fig. 1(a). To optimize coherence and facilitate experimental control, each coupler is also implemented using a tunable transmon^{47,48}. These transmons can be accurately approximated as Duffing oscillators, which is a common model for anharmonic multilevel qubit systems and also applies to capacitively shunted flux qubits^{49,50}.

A versatile tunable coupling scheme—illustrated in the inset of Fig. 1(a)—has been both theoretically proposed and experimentally demonstrated^{40,41}. This architecture consists of a three-body quantum system with pairwise interactions: the leftmost and rightmost anharmonic oscillators act as the sites of EBHM, while the central oscillator serves as a tunable coupler that mediates interactions between the two distant transmons. All three elements are coupled via exchange-type interactions, characterized by coupling strengths g_1 , g_2 , and g_{12} , respectively. The Hamiltonian describing this three-body system is given by:

$$\hat{H} = \sum_{i \in \{1,2,c\}} \left(\omega_i \hat{b}_i^\dagger \hat{b}_i + \frac{\beta_i}{2} \hat{b}_i^\dagger \hat{b}_i^\dagger \hat{b}_i \hat{b}_i \right) - g_{12} (\hat{b}_1 - \hat{b}_1^\dagger) (\hat{b}_2 - \hat{b}_2^\dagger) - \sum_{j \in \{1,2\}} g_j (\hat{b}_j - \hat{b}_j^\dagger) (\hat{b}_c - \hat{b}_c^\dagger), \tag{67}$$

where ω_i are the oscillator frequencies, and β_i denote the anharmonicity of the oscillators. The operators \hat{b}_i^\dagger and \hat{b}_i are the creation and annihilation operators, respectively, defined in the eigenbasis of the corresponding oscillator. We note that the coupler-transmon interactions

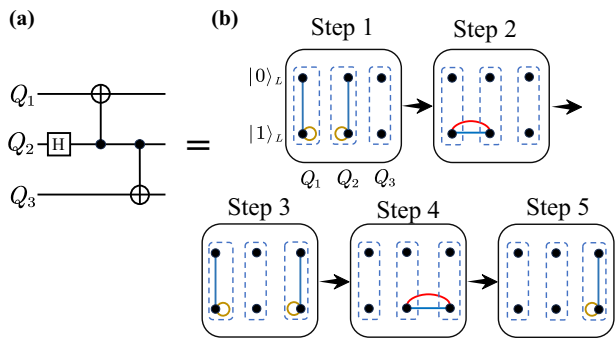


Fig. 10 | GHZ state preparation. **a** Logic circuit diagram for preparing a 3-qubit GHZ state, consisting of a Hadamard gate on Q_2 , followed by two CNOT gates on Q_1, Q_2 and Q_2, Q_3 , respectively. **b** Hamiltonian graphs for preparing the GHZ state using dual-rail encoding. Steps 1 and 3 involve dual-role Hadamard gates, while steps 1 to 3 implement the CNOT gate on Q_1, Q_2 and steps 3 to 5 implement the second CNOT gate on Q_2, Q_3 .

are significantly stronger than the direct transmon-transmon interaction, i.e., $g_1, g_2 \gg g_{12}$, which corresponds to the practical parameter regime for tunable couplers⁴⁰.

The three-body system serves as a unit cell for encoding a logical qubit, defined inside the system’s first excitation subspace. Before proceeding, we derive an effective two-transmon system by applying a block diagonalization transformation to decouple the coupler. We assume that both transmons are far detuned from the coupler and the coupling is dispersive: $\Delta_i \equiv \omega_i - \omega_c \neq 0, g_i \ll |\Delta_i| (i = 1, 2)$. Additionally, we assume that the coupler mode always remains in its ground state, with its excitations not participating in the system dynamics^{34,40,51}.

To a good approximation, the physics of the two-transmon building block is well captured by the EBHM. In the qubit regime, this reduces to a Heisenberg XXZ spin model. For the sake of implementing two-qubit logical gates, we have made a three-level cut-off approximation in deriving the effective Hamiltonian, and the third level will be utilized as a resource for phase accumulation. Fixing the description in the Fock basis and renormalizing the parameters, the effective two-transmon Hamiltonian is derived from Bloch’s theory⁵²:

$$\hat{H}^{\text{eff}} = \sum_{i=1,2} \left(\tilde{\omega}_i \hat{n}_i + \frac{\tilde{\beta}_i}{2} \hat{b}_i^\dagger \hat{b}_i^\dagger \hat{b}_i \hat{b}_i \right) + \tilde{g} (\hat{b}_1^\dagger \hat{b}_2 + \hat{b}_1 \hat{b}_2^\dagger) + \zeta \hat{n}_1 \hat{n}_2, \tag{68}$$

where $\hat{n}_i = \hat{b}_i^\dagger \hat{b}_i$ are the excitation number operators, $\tilde{\omega}_i = \omega_i + g_i^2/\Delta_i$ are the Lamb-shifted frequencies, $\tilde{\beta}_i = \beta_i + 2g_i^2(1/(\Delta_i + \beta_i) - 1/\Delta_i)$ are the shifted anharmonicities, $\tilde{g} = g_1 g_2/\Delta + g_{12}$ is the effective coupling strength, $1/\Delta = (1/\Delta_1 + 1/\Delta_2)/2$, and when $\Delta_1 = \Delta_2, \beta_1 = \beta_2$,

$$\zeta = 4g_1 g_2 g_{12} \left[\frac{1}{\Delta_1^2} - \frac{1}{\Delta_1(\Delta_1 + \beta_1)} \right] + 4g_2^2 g_{12}^2 \left[\frac{2}{\Delta_1^2(2\Delta_1 - \beta_1)} - \frac{1}{\Delta_1^2(\Delta_1 + \beta_1)} \right] \tag{69}$$

represents the ZZ interaction strength. A detailed derivation and the mapping of Eq. (68) to the EBHM Hamiltonian are given in the subsequent subsections. This interaction primarily arises from virtual processes in which two excitations occupy the same transmon or coupler. Typically, the ZZ interaction is an order of magnitude smaller than the coupling strength \tilde{g} . This formalism can be readily extended to model a one-dimensional chain or a two-dimensional array.

The effective exchange coupling g and ZZ interaction ζ between the two transmons can be engineered by appropriately tuning the frequency of the intermediate coupler. As demonstrated in ref. 40, the destructive

interference between the direct transmon-transmon coupling and the coupler-mediated virtual processes enables precise control over the net coupling strength. In particular, by tuning the coupler frequency ω_c , the effective coupling can be selectively switched on or off. Similarly, the ZZ interaction can also be modulated via Eq. (69), as discussed in Section I of the Supplementary Note. Furthermore, the exact results of the effective Hamiltonian can be determined from the method based on the least action principle⁵³. The rich interaction structure of the EBHM enables various types of CTQWs, thereby paving the way for the implementation of logical multiple-qubit gates.

Effective Hamiltonian derivation

In this subsection, we start from a system of three capacitively coupled transmons with the Hamiltonian Eq. (67) introduced in the last subsection, and aim to derive the effective two-body Hamiltonian Eq. (68) by decoupling the coupler. Specifically, most effective parameters are derived in second order in perturbation theory, whereas the effective ZZ coupling is calculated in fourth order.

We now introduce perturbative block diagonalization via Bloch theory. Effective Hamiltonians are essential for capturing low-energy dynamics in complex quantum systems. The Bloch method^{54–56} is a well-established perturbative approach for deriving such Hamiltonians. A refined version by Takayanagi⁵², which we refer to as perturbative block diagonalization (PBD), systematically incorporates block diagonalization techniques while naturally aligning with the least action principle⁵³. Compared to the Schrieffer-Wolff transformation (SWT)⁵⁷, PBD offers direct parameterization of effective interactions, lower computational complexity, and a flexible formalism that accounts for all transition paths between states.

Consider a Hamiltonian H on a D -dimensional Hilbert space \mathcal{H} , decomposed as

$$H = H_0 + V, \tag{70}$$

where H_0 is the unperturbed Hamiltonian and V is the perturbation. We decompose \mathcal{H} into the computational subspace \mathcal{H}_C (of dimension d) and its complement \mathcal{H}_{NC} (of dimension $D - d$), so that an effective Hamiltonian can be constructed within \mathcal{H}_C .

Projectors onto these subspaces are defined by the eigenstates of H_0 :

$$P = \sum_{i=1}^d |i\rangle\langle i|, Q = \sum_{I=d+1}^D |I\rangle\langle I|, \tag{71}$$

with $H_0|i\rangle = \varepsilon_i|i\rangle$ and $H_0|I\rangle = \varepsilon_I|I\rangle, |i\rangle \in \mathcal{H}_C$ and $|I\rangle \in \mathcal{H}_{NC}$. For eigenstates $|\Psi_k\rangle$ of H with eigenvalues E_k (for $k = 1, \dots, d$), we decompose

$$|\Psi_k\rangle = P|\Psi_k\rangle + Q|\Psi_k\rangle \equiv |\phi_k\rangle + |\Phi_k\rangle. \tag{72}$$

Since this construction does not explicitly enforce unitarity, the states $\{|\phi_k\rangle\}$ may not be orthonormal, and H_{eff} can be non-Hermitian. To restore Hermiticity while preserving the essential physics, a symmetrization is applied⁵⁸:

$$H_{\text{eff}}^{\text{Herm}} = \frac{1}{2}(H_{\text{eff}} + H_{\text{eff}}^\dagger). \tag{73}$$

The effective Hamiltonian is expressed as

$$H_{\text{eff}} = PH_0P + V_{\text{eff}}, \tag{74}$$

with $V_{\text{eff}} = PV_{\text{eff}}P$ representing effective interactions. Up to fourth order⁵², the expansion is given by

$$\begin{aligned} V_{\text{eff}}^{(1)} &= PVP, \\ V_{\text{eff}}^{(2)} &= P[V(V)]P, \\ V_{\text{eff}}^{(3)} &= P[V(V(V)) - V((V)V)]P, \\ V_{\text{eff}}^{(4)} &= P[V(V(V(V))) - V(V((V)V)) - V((V(V)V)) \\ &\quad + V(((V)V)V) - V((V)V(V))]P. \end{aligned} \tag{75}$$

In this notation, the superoperator (V) is defined as

$$[(V)]_{ji} = \frac{1}{\epsilon_j - \epsilon_i} \langle I|V|i\rangle, \tag{76}$$

where $|i\rangle$ and $|I\rangle$ are eigenstates of H_0 with energies ϵ_i and ϵ_j , respectively.

To go beyond the rotating-wave approximation (RWA), we first derive a second-order effective Hamiltonian that systematically incorporates the leading contributions from counter-rotating terms. These contributions are absorbed into renormalized mode frequencies and interaction strengths. The full results are provided in Section VI of the Supplementary Note.

The resulting effective Hamiltonian takes the form

$$\begin{aligned} \hat{H}_{\text{eff}} &= \sum_{i \in \{1,2,c\}} \left(\tilde{\omega}_i \hat{b}_i^\dagger \hat{b}_i + \frac{\beta_i}{2} \hat{b}_i^\dagger \hat{b}_i^\dagger \hat{b}_i \hat{b}_i \right) + \tilde{g}_{12} \left(\hat{b}_1 \hat{b}_2^\dagger + \hat{b}_1^\dagger \hat{b}_2 \right) \\ &\quad + \sum_{j \in \{1,2\}} \tilde{g}_j \left(\hat{b}_j \hat{b}_c^\dagger + \hat{b}_j^\dagger \hat{b}_c \right), \end{aligned} \tag{77}$$

where the tilded parameters $\tilde{\omega}_i, \tilde{g}_j, \tilde{g}_{12}$ encode renormalizations due to virtual counter-rotating processes. For simplicity of notation, we drop the tilde in what follows.

Next, we detail the second step in deriving the effective two-transmon Hamiltonian: the decoupling of the coupler mode. By operating in the dispersive regime (i.e., $|g_j/\Delta_j| \ll 1$ with $\Delta_j \equiv \omega_j - \omega_c$ for $j \in \{1, 2\}$) and noting that the direct transmon-transmon coupling g_{12} is typically much smaller than the transmon-coupler couplings g_j , we can perform a block-diagonalization to isolate the low-energy subspace in which the coupler remains in its ground state. This procedure yields an effective two-transmon Hamiltonian that retains only the relevant interactions.

We begin by decomposing the full Hilbert space into excitation-number subspaces, $\mathcal{H} = \bigoplus_i \mathcal{H}_i$, where \mathcal{H}_i denotes the i -excitation subspace. We then partition the full Hamiltonian into an unperturbed part and a perturbation. Specifically, we define

$$\hat{H}_0 = \sum_{i \in \{1,2,c\}} \left(\omega_i \hat{b}_i^\dagger \hat{b}_i + \frac{\beta_i}{2} \hat{b}_i^\dagger \hat{b}_i^\dagger \hat{b}_i \hat{b}_i \right) + g_{12} \left(\hat{b}_1 \hat{b}_2^\dagger + \hat{b}_1^\dagger \hat{b}_2 \right), \tag{78}$$

which contains the local energies, anharmonicities, and the direct transmon-transmon coupling, and

$$V = \sum_{j \in \{1,2\}} g_j \left(\hat{b}_j \hat{b}_c^\dagger + \hat{b}_j^\dagger \hat{b}_c \right), \tag{79}$$

which describes the transmon-coupler interactions.

We perform a perturbative block-diagonalization transformation that retains only the low-energy sector with the coupler in its ground state. Let H_{eff} denote the resulting effective Hamiltonian in this reduced Hilbert space

\mathcal{H}_C . We then define the effective hopping and ZZ interaction strengths by

$$\begin{aligned} \tilde{g} &= \langle 100|H_{\text{eff}}|001\rangle, \\ \zeta &= \langle 101|H_{\text{eff}}|101\rangle - \langle 100|H_{\text{eff}}|100\rangle - \langle 001|H_{\text{eff}}|001\rangle \\ &\quad + \langle 000|H_{\text{eff}}|000\rangle. \end{aligned} \tag{80}$$

In these expressions, the labels on the kets (e.g., $|100\rangle$) denote the occupation numbers of the two transmons and the coupler as $|Q_1, C, Q_2\rangle$.

The one-excitation manifold is decomposed as $\mathcal{H}_1 = \mathcal{H}_{1,C} \oplus \mathcal{H}_{1,NC}$

$$\mathcal{H}_{1,C} = \text{span}\{|100\rangle, |001\rangle\}, \mathcal{H}_{1,NC} = |010\rangle. \tag{81}$$

There is only a single virtual transition mediated by the coupler

$$|100\rangle \xrightarrow{g_1} |010\rangle \xrightarrow{g_2} |001\rangle$$

[contribute to the effective hopping. Following the second-order result in Eq. (75), we have

$$\tilde{g} = g_{12} + \frac{g_1 g_2}{2} \left(\frac{1}{\Delta_1} + \frac{1}{\Delta_2} \right). \tag{82}$$

If taking into account the counter-rotating terms,

$$\tilde{g} = g_{12} + \frac{g_1 g_2}{2} \left(\frac{1}{\Delta_1} + \frac{1}{\Delta_2} \right) - \frac{g_1 g_2}{2} \left(\frac{1}{\Sigma_1} + \frac{1}{\Sigma_2} \right), \tag{83}$$

where $\Sigma_i = \omega_i + \omega_c$, $i \in \{1, 2\}$.

In addition, there is a virtual transition mediated by the coupler to renormalize the transmon frequency up to second-order:

$$|100\rangle \xrightarrow{g_1} |010\rangle \xrightarrow{g_1} |100\rangle,$$

giving a frequency shift g_1^2/Δ_1 and $\tilde{\omega}_1 = \omega_1 + g_1^2/\Delta_1$. Similar reasoning gives $\tilde{\omega}_2 = \omega_2 + g_2^2/\Delta_2$. Therefore,

$$\tilde{\omega}_j = \omega_j + \frac{g_j^2}{\Delta_j}, j \in \{1, 2\}. \tag{84}$$

The double-excitation manifold is decomposed as $\mathcal{H}_2 = \mathcal{H}_{2,C} \oplus \mathcal{H}_{2,NC}$, with

$$\begin{aligned} \mathcal{H}_{2,C} &= \text{span}\{|200\rangle, |101\rangle, |002\rangle\}, \\ \mathcal{H}_{2,NC} &= \text{span}\{|110\rangle, |020\rangle, |011\rangle\}. \end{aligned} \tag{85}$$

The main part of ZZ coupling arises from the third- and the fourth-order. We have identified four representative virtual processes involving the frequency shift of $|101\rangle$, and they are not seen from the states $|100\rangle$ and $|001\rangle$.

- (1) $|101\rangle \xrightarrow{g_1} |011\rangle \xrightarrow{g_{12}} |110\rangle \xrightarrow{g_2} |101\rangle,$
- (2) $|101\rangle \xrightarrow{\sqrt{2}g_{12}} |200\rangle \xrightarrow{\sqrt{2}g_1} |110\rangle \xrightarrow{g_2} |101\rangle,$
- (3) $|101\rangle \xrightarrow{g_2} |110\rangle \xrightarrow{\sqrt{2}g_1} |020\rangle \xrightarrow{\sqrt{2}g_1} |110\rangle \xrightarrow{g_2} |101\rangle,$
- (4) $|101\rangle \xrightarrow{g_2} |110\rangle \xrightarrow{\sqrt{2}g_1} |200\rangle \xrightarrow{\sqrt{2}g_1} |110\rangle \xrightarrow{g_2} |101\rangle.$

Similar to the one-excitation case, we can calculate the values of each process using Eq. (75), giving

- (1) $\frac{g_1 g_2 g_{12}}{\Delta_1 \Delta_2},$
- (2) $-\frac{2g_1 g_2 g_{12}}{(\Delta_1 + \beta_1) \Delta_2},$
- (3) $\frac{2g_1^2 g_2^2}{(\Delta_1 + \Delta_2 - \beta_2) \Delta_2^2},$
- (4) $-\frac{2g_1^2 g_2^2}{(\Delta_1 + \beta_1) \Delta_2^2}.$

Finally, summarizing all the possible processes, we obtain

$$\begin{aligned} \zeta = & g_1 g_2 g_{12} \left(\frac{4}{\Delta_1 \Delta_2} - \frac{2}{(\Delta_1 + \beta_1) \Delta_2} - \frac{2}{\Delta_1 (\Delta_2 + \beta_2)} \right) \\ & + g_1^2 g_2^2 \left(\left(\frac{4}{\Delta_1 \Delta_2} + \frac{2}{\Delta_1^2} + \frac{2}{\Delta_2^2} \right) \frac{1}{\Delta_1 + \Delta_2 - \beta_c} \right) \\ & - g_1^2 g_2^2 \left(\frac{2}{(\Delta_1 + \beta_1) \Delta_2^2} + \frac{2}{(\Delta_2 + \beta_2) \Delta_1^2} \right). \end{aligned} \quad (86)$$

In addition, there is a virtual transition mediated by the coupler to renormalize the energy of state $|200\rangle$ up to the second-order:

$$|200\rangle \overset{\sqrt{2}g_1}{\leftrightarrow} |110\rangle \overset{\sqrt{2}g_1}{\leftrightarrow} |200\rangle,$$

which give rise to $\tilde{\beta}_1 = \beta_1 + 2g_1^2 \left(\frac{1}{\Delta_1 + \beta_1} - \frac{1}{\Delta_1} \right)$. Similar reasoning gives $\tilde{\beta}_2$, and they together indicate

$$\tilde{\beta}_j = \beta_j + 2g_j^2 \left(\frac{1}{\Delta_j + \beta_j} - \frac{1}{\Delta_j} \right), j \in \{1, 2\}. \quad (87)$$

Derivation of the extended Bose-Hubbard model in a rotating frame

In this subsection, we map the effective Hamiltonian Eq. (68) to the form of the EBHM Eq. (1) by employing a rotating frame transformation. Starting from an effective two-body Hamiltonian that includes on-site energies, anharmonicities, hopping, and ZZ interactions, we remove the large energy scales associated with the oscillator frequencies. This transformation yields a Hamiltonian where the remaining terms are on the order of MHz.

We begin with the effective Hamiltonian for the two-body system:

$$\begin{aligned} \hat{H}^{\text{eff}} = & \sum_{i=1,2} \left(\tilde{\omega}_i \hat{n}_i + \frac{\tilde{\beta}_i}{2} \hat{b}_i^\dagger \hat{b}_i \hat{b}_i^\dagger \hat{b}_i \right) + \tilde{g} \left(\hat{b}_1^\dagger \hat{b}_2 + \hat{b}_1 \hat{b}_2^\dagger \right) \\ & + \zeta \hat{n}_1 \hat{n}_2, \end{aligned} \quad (88)$$

where $\tilde{\omega}_i$ (of order GHz) are the effective mode frequencies, $\tilde{\beta}_i$ are the anharmonicities, \tilde{g} is the effective hopping strength, and ζ denotes the ZZ interaction strength. Since the interactions are much smaller (order MHz) than the mode frequencies, we employ a rotating frame transformation to eliminate these large energy scales.

Defining the unitary operator

$$\hat{U}_R(t) = e^{-i\tilde{\omega}_1(\hat{n}_1 + \hat{n}_2)t}, \quad (89)$$

the Hamiltonian in the rotating frame is given by

$$\hat{H}_R = \hat{U}_R^\dagger \hat{H}^{\text{eff}} \hat{U}_R + i \frac{d\hat{U}_R^\dagger}{dt} \hat{U}_R. \quad (90)$$

Carrying out this transformation, we obtain

$$\begin{aligned} \hat{H}_R = & \Delta_{21} \hat{n}_2 + \sum_{i=1,2} \frac{\tilde{\beta}_i}{2} \hat{b}_i^\dagger \hat{b}_i \hat{b}_i^\dagger \hat{b}_i + \tilde{g} \left(\hat{b}_1^\dagger \hat{b}_2 + \hat{b}_1 \hat{b}_2^\dagger \right) \\ & + \zeta \hat{n}_1 \hat{n}_2, \end{aligned} \quad (91)$$

where $\Delta_{21} = \tilde{\omega}_2 - \tilde{\omega}_1$ is on the order of MHz.

To express the Hamiltonian in the conventional EBHM form, we rewrite it as

$$\hat{H} = -J \sum_{\langle i,j \rangle} \hat{c}_i^\dagger \hat{c}_j + \frac{U}{2} \sum_i \hat{n}_i (\hat{n}_i - 1) - \sum_i \mu_i \hat{n}_i + V \sum_i \hat{n}_i \hat{n}_{i+1}, \quad (92)$$

with the parameter identifications:

$$J = -\tilde{g}, U = \tilde{\beta}_1 = \tilde{\beta}_2, \mu_1 = 0, \mu_2 = -\Delta_{21}, V = \zeta. \quad (93)$$

Thus, the effective Hamiltonian in the rotating frame maps directly onto the EBHM, with all parameters now on the energy scale of MHz.

This derivation highlights how a rotating frame transformation can effectively remove large mode energies and reveal the low-energy interactions relevant for quantum simulation, thereby providing a clear pathway to implementing the EBHM with superconducting transmon systems.

Data availability

Code and data are available via: <https://github.com/QDynamics/CTQW-on-dual-railqubits>.

Code availability

Code and data are available via: <https://github.com/QDynamics/CTQW-on-dual-railqubits>.

Received: 15 January 2025; Accepted: 13 November 2025;

Published online: 17 January 2026

References

1. Kubica, A. et al. Erasure qubits: overcoming the t_1 limit in superconducting circuits. *Phys. Rev. X* **13**, 041022 (2023).
2. Shim, Y.-P. & Tahan, C. Semiconductor-inspired design principles for superconducting quantum computing. *Nat. Commun.* **7**, 11059 (2016).
3. Teoh, J. D. et al. Dual-rail encoding with superconducting cavities. *Proc. Natl. Acad. Sci. USA* **120**, e2221736120 (2023).
4. Campbell, D. L. et al. Universal nonadiabatic control of small-gap superconducting qubits. *Phys. Rev. X* **10**, 041051 (2020).
5. Levine, H. et al. Demonstrating a long-coherence dual-rail erasure qubit using tunable transmons. *Phys. Rev. X* **14**, 011051 (2024).
6. Chou, K. S. et al. A superconducting dual-rail cavity qubit with erasure-detected logical measurements. *Nat. Phys.* **20**, 1454–1460 (2024).
7. Koottandavida, A. et al. Erasure detection of a dual-rail qubit encoded in a double-post superconducting cavity. *Phys. Rev. Lett.* **132**, 180601 (2024).
8. Weiss, D., Puri, S. & Girvin, S. Quantum random access memory architectures using 3d superconducting cavities. *PRX Quantum* **5**, 020312 (2024).
9. Wong, T. G. Isolated vertices in continuous-time quantum walks on dynamic graphs. *Phys. Rev. A* **100**, 062325 (2019).
10. Chawla, P., Singh, S., Agarwal, A., Srinivasan, S. & Chandrashekar, C. Multi-qubit quantum computing using discrete-time quantum walks on closed graphs. *Sci. Rep.* **13**, 12078 (2023).
11. Farhi, E. & Gutmann, S. Quantum computation and decision trees. *Phys. Rev. A* **58**, 915 (1998).
12. Childs, A. M., Farhi, E. & Gutmann, S. An example of the difference between quantum and classical random walks. *Quantum Inf. Process.* **1**, 35–43 (2002).
13. Childs, A. M. et al. Exponential algorithmic speedup by a quantum walk. In *Proceedings of the thirty-fifth annual ACM symposium on Theory of Computing*, 59–68 (2003).
14. Childs, A. M. *Quantum information processing in continuous time*. Ph.D. thesis, Massachusetts Institute of Technology (2004).
15. Peruzzo, A. et al. Quantum walks of correlated photons. *Science* **329**, 1500–1503 (2010).
16. Yan, Z. et al. Strongly correlated quantum walks with a 12-qubit superconducting processor. *Science* **364**, 753–756 (2019).
17. Gong, M. et al. Quantum walks on a programmable two-dimensional 62-qubit superconducting processor. *Science* **372**, 948–952 (2021).

18. Lahini, Y. et al. Quantum walk of two interacting bosons. *Phys. Rev. A-At., Mol. Opt. Phys.* **86**, 011603 (2012).
19. Siloi, I. et al. Noisy quantum walks of two indistinguishable interacting particles. *Phys. Rev. A* **95**, 022106 (2017).
20. Lewis, D., Benhemou, A., Feinstein, N., Banchi, L. & Bose, S. Optimal quantum spatial search with one-dimensional long-range interactions. *Phys. Rev. Lett.* **126**, 240502 (2021).
21. Xing, F., Wei, Y. & Liao, Z. Quantum search in many-body interacting systems with long-range interactions. *Phys. Rev. A* **109**, 052435 (2024).
22. Wong, T. G. Spatial search by continuous-time quantum walk with multiple marked vertices. *Quantum Inf. Process.* **15**, 1411–1443 (2016).
23. Wong, T. G. Grover search with lackadaisical quantum walks. *J. Phys. A: Math. Theor.* **48**, 435304 (2015).
24. Wang, S.-M., Qu, Y.-J., Wang, H.-W., Chen, Z. & Ma, H.-Y. Multiparticle quantum walk-based error correction algorithm with two-lattice Bose–Hubbard model. *Front. Phys.* **10**, 1016009 (2022).
25. Childs, A. M., Gosset, D. & Webb, Z. Universal computation by multiparticle quantum walk. *Science* **339**, 791–794 (2013).
26. Underwood, M. S. & Feder, D. L. Bose–Hubbard model for universal quantum-walk-based computation. *Phys. Rev. A* **85**, 052314 (2012).
27. e Silva, L. L. & Brod, D. J. Two-particle scattering on non-translation invariant line lattices. *Quantum* **8**, 1308 (2024).
28. Asaka, R., Sakai, K. & Yahagi, R. Two-level quantum walkers on directed graphs. I. Universal quantum computing. *Phys. Rev. A* **107**, 022415 (2023).
29. Lahini, Y., Steinbrecher, G. R., Bookatz, A. D. & Englund, D. Quantum logic using correlated one-dimensional quantum walks. *npj Quantum Inf.* **4**, 2 (2018).
30. Dutta, O. et al. Non-standard Hubbard models in optical lattices: a review. *Rep. Prog. Phys.* **78**, 066001 (2015).
31. Baier, S. et al. Extended Bose–Hubbard models with ultracold magnetic atoms. *Science* **352**, 201–205 (2016).
32. Browaeys, A. & Lahaye, T. Many-body physics with individually controlled Rydberg atoms. *Nat. Phys.* **16**, 132–142 (2020).
33. Ebadi, S. et al. Quantum optimization of maximum independent set using Rydberg atom arrays. *Science* **376**, 1209–1215 (2022).
34. Kounalakis, M., Dickel, C., Bruno, A., Langford, N. & Steele, G. Tuneable hopping and nonlinear cross-kerr interactions in a high-coherence superconducting circuit. *npj Quantum Inf.* **4**, 38 (2018).
35. Lagoin, C. et al. Extended Bose–Hubbard model with dipolar excitons. *Nature* **609**, 485–489 (2022).
36. Berke, C., Varvelis, E., Trebst, S., Altland, A. & DiVincenzo, D. P. Transmon platform for quantum computing challenged by chaotic fluctuations. *Nat. Commun.* **13**, 2495 (2022).
37. Zhang, X., Kim, E., Mark, D. K., Choi, S. & Painter, O. A superconducting quantum simulator based on a photonic-bandgap metamaterial. *Science* **379**, 278–283 (2023).
38. Raventós, D., Graß, T., Lewenstein, M. & Juliá-Díaz, B. Cold bosons in optical lattices: a tutorial for exact diagonalization. *J. Phys. B At. Mol. Opt. Phys.* **50**, 113001 (2017).
39. Benatti, F., Floreanini, R., Franchini, F. & Marzolino, U. Entanglement in indistinguishable particle systems. *Phys. Rep.* **878**, 1–27 (2020).
40. Yan, F. et al. Tunable coupling scheme for implementing high-fidelity two-qubit gates. *Phys. Rev. Appl.* **10**, 054062 (2018).
41. Sung, Y. et al. Realization of high-fidelity cz and z z-free iswap gates with a tunable coupler. *Phys. Rev. X* **11**, 021058 (2021).
42. Nielsen, M. A. & Chuang, I. L. *Quantum computation and quantum information*, vol. 2 (Cambridge University Press, 2001).
43. DiVincenzo, D. P. Two-bit gates are universal for quantum computation. *Phys. Rev. A* **51**, 1015 (1995).
44. Blais, A., Grimsmo, A. L., Girvin, S. M. & Wallraff, A. Circuit quantum electrodynamics. *Rev. Mod. Phys.* **93**, 025005 (2021).
45. Mundada, P., Zhang, G., Hazard, T. & Houck, A. Suppression of qubit crosstalk in a tunable coupling superconducting circuit. *Phys. Rev. Appl.* **12**, 054023 (2019).
46. Pedersen, L. H., Møller, N. M. & Mølmer, K. Fidelity of quantum operations. *Phys. Lett. A* **367**, 47–51 (2007).
47. Koch, J. et al. Charge-insensitive qubit design derived from the Cooper pair box. *Phys. Rev. A-At., Mol. Opt. Phys.* **76**, 042319 (2007).
48. Hutchings, M. et al. Tunable superconducting qubits with flux-independent coherence. *Phys. Rev. Appl.* **8**, 044003 (2017).
49. Steffen, M. et al. High-coherence hybrid superconducting qubit. *Phys. Rev. Lett.* **105**, 100502 (2010).
50. Yan, F. et al. The flux qubit revisited to enhance coherence and reproducibility. *Nat. Commun.* **7**, 12964 (2016).
51. Luo, K. et al. Experimental realization of two qutrits gate with tunable coupling in superconducting circuits. *Phys. Rev. Lett.* **130**, 030603 (2023).
52. Takayanagi, K. Effective interaction in unified perturbation theory. *Ann. Phys.* **364**, 200–247 (2016).
53. Cederbaum, L., Schirmer, J. & Meyer, H.-D. Block diagonalisation of hermitian matrices. *J. Phys. A: Math. Gen.* **22**, 2427 (1989).
54. Bloch, C. Sur la théorie des perturbations des états liés. *Nucl. Phys.* **6**, 329–347 (1958).
55. Killingbeck, J. P. & Jolicard, G. The Bloch wave operator: generalizations and applications: Part I. The time-independent case. *J. Phys. A Math. Gen.* **36**, R105 (2003).
56. Shavitt, I. & Bartlett, R. J. *Many-body methods in chemistry and physics: MBPT and coupled-cluster theory* (Cambridge University Press, 2009).
57. Bravyi, S., DiVincenzo, D. P. & Loss, D. Schrieffer–wolff transformation for quantum many-body systems. *Ann. Phys.* **326**, 2793–2826 (2011).
58. Richert, J., Schucan, T., Simbel, M. & Weidenmüller, H. A comparison between various expressions for effective interactions and operators in nuclei. *Ann. Phys.* **96**, 139–157 (1976).

Acknowledgements

This work was supported by the Key-Area Research and Development Program of Guang-Dong Province (Grant No. 2018B030326001), and the Science, Technology and Innovation Commission of Shenzhen Municipality (JCYJ20170412152620376, KYTDPT20181011104202253), and the Shenzhen Science and Technology Program (KQTD20200820113010023).

Author contributions

The manuscript was collaboratively authored by all contributors. HY Guan and Y Li made equal contributions to the derivation, the execution of numerical simulations, and the plotting of figures. The project was initiated, overseen, and coordinated by XH Deng.

Competing interests

The authors declare no competing interests.

Additional information

Supplementary information The online version contains supplementary material available at <https://doi.org/10.1038/s41534-025-01147-1>.

Correspondence and requests for materials should be addressed to Xiu-Hao Deng.

Reprints and permissions information is available at <http://www.nature.com/reprints>

Publisher's note Springer Nature remains neutral with regard to jurisdictional claims in published maps and institutional affiliations.

Open Access This article is licensed under a Creative Commons Attribution-NonCommercial-NoDerivatives 4.0 International License, which permits any non-commercial use, sharing, distribution and reproduction in any medium or format, as long as you give appropriate credit to the original author(s) and the source, provide a link to the Creative Commons licence, and indicate if you modified the licensed material. You do not have permission under this licence to share adapted material derived from this article or parts of it. The images or other third party material in this article are included in the article's Creative Commons licence, unless indicated otherwise in a credit line to the material. If material is not included in the article's Creative Commons licence and your intended use is not permitted by statutory regulation or exceeds the permitted use, you will need to obtain permission directly from the copyright holder. To view a copy of this licence, visit <http://creativecommons.org/licenses/by-nc-nd/4.0/>.

© The Author(s) 2026